Diamonds from the Machado River alluvial deposit, Rondônia, Brazil, derived from both lithospheric and sublithospheric mantle

A.D. Burnham[a1], G.P. Bulanova[a], C.B. Smith[a], S.C. Whitehead[a], S.C. Kohn[a], L. Gobbo[b], M.J. Walter[a]
a – School of Earth Sciences, Wills Memorial Building, University of Bristol, BS8 1RJ, United Kingdom
b – Rio Tinto Desenvolvimentos Minerais Ltda., Brasília, Brazil
1 (corresponding author) – present address: Research School of Earth Sciences, Australian National University, Acton, ACT 2601, Australia. Email: antony.burnham@anu.edu.au

Abstract
Diamonds from the Machado River alluvial deposit have been characterised on the basis of external morphology, internal textures, carbon isotopic composition, nitrogen concentration and aggregation state and mineral inclusion chemistry. Variations in morphology and features of abrasion suggest some diamonds have been derived directly from local kimberlites, whereas others have been through extensive sedimentary recycling. On the basis of mineral inclusion compositions, both lithospheric and sublithospheric diamonds are present at the deposit. The lithospheric diamonds have clear layer-by-layer octahedral and/or cuboid internal growth zonation, contain measurable nitrogen and indicate a heterogeneous lithospheric mantle beneath the region. The sublithospheric diamonds show a lack of regular sharp zonation, do not contain detectable nitrogen, are isotopically heavy ($\delta^{13}C_{PDB}$ predominantly -0.7 – -5.5) and contain inclusions of ferropericlase, former bridgmanite, majoritic garnet and former $CaSiO_3$-perovskite. This suggests source lithologies that are Mg- and Ca-rich, probably including carbonates and serpentinites, subducted to lower mantle depths. The studied suite of sublithospheric diamonds has many similarities to the alluvial diamonds from Kankan, Guinea, but has more extreme variations in mineral inclusion chemistry. Of all superdeep diamond suites yet discovered, Machado River represents an end-member in terms of either the compositional range of materials being subducted to Transition Zone and lower mantle or the process by which materials are transferred from the subducted slab to the diamond-forming region.

Keywords
bridgmanite; majorite; subduction; carbon; superdeep; diamond

1. Introduction

Although the vast majority of the world's diamonds are characterised by being inclusion-free (96 - 99 %), and ~ 28 % of inclusions are trace-element poor olivines and chrome spinels (Stachel and Harris, 2008), they have continued to draw keen interest from petrologists and geochemists. While diamonds undoubtedly offer a selective view of the deep Earth, in particular of the highly depleted Archaean cratonic mantle (Stachel and Harris, 2008), the fidelity with which the chemistry of inclusions is preserved makes them a valuable scientific resource. Around 5 – 10 % of diamonds are derived from beneath the base of the lithosphere (i.e. sublithospheric, or "superdeep") and are direct evidence of the mixing and recycling processes that lead to mantle-derived lavas with diverse isotopic and elemental characteristics (e.g. Pietruszka et al., 2013).

The minerals that are included in these superdeep diamonds may only represent a single fragment of a single geological event in a rock's life cycle, but this information is essential for reconstructing the geological history of subducted material. Variations in the characteristics of diamonds and their inclusions within and between localities testify about the spatial and/or temporal variability of the source region: they reveal, for example, the presence of multiple

lithologies and a wide range of carbon isotopes in the Transition Zone and lower mantle (e.g. Stachel et al., 2001; Harte, 2010). A combination of results obtained from superdeep diamond studies and experiments constrains the extent to which C might be recycled into the lower mantle (e.g. Thomson et al., 2016). Additional well-characterised suites of superdeep diamonds are essential to establishing both the average and the range of lithologies present in the deep mantle.

The Juina region in Mato Grosso State, Brazil, has been studied extensively because of the high abundance of sublithospheric diamonds there, both in kimberlite pipes (e.g. Kaminsky et al., 2009; Bulanova et al., 2010; Thomson et al., 2014a) and in alluvial deposits (e.g. Harte et al., 1999; Kaminsky et al., 2001; Hayman et al., 2005; Zedgenizov et al., 2014). These extraordinary diamonds have a wide range of carbon isotopic compositions, -28.3 – +0.4 ‰, and contain a variety of mineral inclusions, often rich in incompatible elements (e.g. the rare earth elements (REE), Ti, Zr, Na and K). Many of these diamonds appear to have formed by redox freezing of a slab-derived carbonatite melt as it percolated into the highly reduced deep mantle (Walter et al., 2008; Bulanova et al., 2010; Walter et al., 2011; Burnham et al., 2015; Thomson et al., 2016; Thomson et al., *this issue*). The kimberlites of the Juina region were emplaced at ~ 92 – 95 Ma (Heaman et al., 1998).

The Machado River alluvial diamond deposit, situated in Rondônia State, Brazil, lies approximately 250 km west of the Juina region (Fig. 1). Numerous kimberlites with Triassic ages are situated upstream of the deposit (Masun and Scott Smith, 2008), as is the Cretaceous Parecis Formation, which consists of diamondiferous sandstones and conglomerates. The Machado River deposit has previously been described as containing both lithospheric and superdeep diamonds (Bulanova et al., 2008). Further investigation has confirmed this view. Here, we present our extended data set on the external and internal morphology, mineralogy and geochemistry of Machado River diamonds, including the remarkable superdeep population, and suggest a model for their formation. We also discuss the heterogeneous nature of the Machado River diamonds and their possible primary sources.

2. Methods

Diamonds were examined under a binocular microscope to observe morphological features (size, colour, shape and surface textures); of these, 45 stones were selected for further study and prepared for analysis by polishing along the dodecahedral plane on a diamond-impregnated steel scaife. Diamonds and their inclusions were studied by cathodoluminescence (CL) and in back-scattered electron mode using a Hitachi S-3500N scanning electron microscope. Energy dispersive spectroscopy (EDS) allowed preliminary estimates of mineral compositions.

Wavelength dispersive electron probe microanalysis (EPMA) of the inclusions was performed using a Cameca SX-100 electron probe at the University of Bristol. Calibration standards were a mixture of natural minerals and synthetic oxides and metals, and the data were processed using the PAP matrix correction.

Secondary ion mass spectrometry (SIMS) analysis of trace elements in the inclusions was performed at the Edinburgh Ion Microprobe Facility (EIMF) using the ims-4f ion probe by the method described in Bulanova et al. (2010), with additional analysis of Co, Ni, Cu, Zn and Ga at high mass resolution using the Cameca 1270 ion probe. Si was used as the internal standard for all minerals except ferropericlase (Mg). Secondary standards were used to validate interference corrections. No secondary standard was available for ferropericlase and the results are likely to have larger errors.

Laser ablation inductively coupled mass spectrometry (LA-ICP-MS) of one inclusion was performed using a 193 nm excimer laser and a HelEx ablation cell coupled to an Agilent 7700 mass spectrometer with He as the carrier gas. A background was collected for 20 s followed by a usable ablation period of 30 s. The isotopes measured were ^{7}Li, ^{23}Na, ^{25}Mg, ^{27}Al, ^{29}Si, ^{31}P, ^{39}K, ^{43}Ca, ^{45}Sc, ^{47}Ti, ^{75}As, ^{85}Rb, ^{88}Sr, ^{89}Y, ^{90}Zr, ^{93}Nb, ^{133}Cs, ^{137}Ba, ^{139}La, ^{140}Ce, ^{141}Pr, ^{146}Nd, ^{147}Sm, ^{153}Eu, ^{157}Gd, ^{159}Tb, ^{163}Dy, ^{165}Ho, ^{166}Er, ^{169}Tm, ^{172}Yb, ^{175}Lu, ^{178}Hf, ^{181}Ta, ^{232}Th and ^{238}U. NIST610 glass was used as an external standard before and after the analyses, and Si (determined by EPMA) was used as the internal standard.

Carbon isotope ratios were measured using two instruments: (1) a Cameca 1270 ion probe at EIMF following the method described in Burnham et al. (2015); (2) the SHRIMP SI at the Australian National University with a beam current of 15 nA, analytical spot size of ~30 μm diameter and calibrating relative to a selection of standards. Diamond P28 was analysed using both instruments to ensure inter-comparability of the two data sets. Carbon isotopic compositions were found to differ systematically depending on the standard used.

Fourier transform infrared spectroscopy (FTIR) was performed at the University of Bristol using a Thermo Scientific iN10MX microscope. The spectra were recorded using a liquid N_2 cooled detector at a resolution of 2 cm^{-1}. After normalising the spectra to an absorbance of 12.3 cm^{-1} at 1992 cm^{-1} (Mendelssohn and Milledge, 1995), the concentrations of nitrogen stored as A- and B-defects were calculated using the spreadsheet caxbd97.xls (D. Fisher, *pers. comm.*).

The inclusions in diamond P33 were examined by Raman spectroscopy using a Renishaw inVia confocal microscope at the Australian National University, using 532 and 633 nm laser wavelengths. Mineral identifications were made by comparison to the RRUFF database.

The affinities of the diamonds (peridotitic lithospheric, eclogitic lithospheric or superdeep) were determined by a combination of mineral inclusion chemistry and FTIR characteristics.

3. Results

3.1 External morphology of the diamonds

The Machado River diamonds studied range in size from 1.4 – 6 mm diameter. Typical morphologies are shown in Fig. 2. Dodecahedral diamond shapes predominate (Fig. 2a). 70% of Machado diamonds show features such as rhombic cracks (Fig. 2b) and percussion marks (Fig. 2c), which have previously demonstrated in the literature to be caused by abrasion (Robinson, 1979; Afanasiev et al., 2000). Green and brown radiation spots on the diamond surfaces (Fig. 2d) are common, indicating recycling from secondary placers that were buried (palaeocollectors). 30% of stones are represented by white octahedrons which show little resorption and transportation wear suggesting more than one primary source for the alluvial stones.

3.2 Internal structure of the diamonds

The diamonds display a variety of internal structures. Sharp, often oscillatory zoning suggestive of an octahedral growth habit is common in the lithospheric peridotitic and eclogitic diamonds, as is sector zoning (Fig. 3a). In contrast the superdeep diamonds tend to have one or more of the following features: no obvious growth zonation, possible growth-related textures that are diffuse and/or geometrically complex, and textures that are more likely deformation-related (Fig. 3b-d).

3.3 Mineralogy and compositions of the inclusions

Of the 45 diamonds studied, 28 contained mineral inclusions. The majority of inclusions were homogeneous and single-phase, the commonest being olivine, orthopyroxene and ferropericlase; five diamonds contained two-phase inclusions, two of which are illustrated in Fig. 4. The major element compositions of the silicate inclusions are given in Table 1, and the compositions of the sulphide inclusions are given in Table 2. Trace element data as determined by SIMS and LA-ICP-MS are reported in Tables 3 and 4 respectively.

In many superdeep diamonds, the inclusions are composite (polyphase) but inferred to have formed as single-phase minerals that have subsequently retrogressed to the observed assemblage (e.g. Hayman et al., 2005; Bulanova et al, 2010; Thomson et al., 2014a; Burnham et al., 2015). The bulk composition of such former single-phase inclusions can be estimated approximately by taking the average of the constituent phases, weighted by the areal proportions as measured from SEM images. Such estimates are prone to large errors because of the large size of the individual phases relative to the total inclusion: the calculated bulk composition is very sensitive to the level to which the inclusion is polished, which could entirely miss some exsolved phases not exposed to the surface. Therefore, the bulk inclusion compositions reported in Table 1 are approximations only.

Most mineral inclusion species have a wide range of compositions from diamond to diamond. The Mg# (= 100×Mg/(Mg+Fe) on a molar basis) of the mineral inclusions ranges from 88.2 – 94.8 for olivine, 86.9 – 97.0 for orthopyroxene, 73.1 – 95.8 for clinopyroxene and 59.7 – 89.5 for garnet. The Al, Ca and Ni concentrations in orthopyroxene vary markedly. Clinopyroxene was observed in seven diamonds, sometimes as part of composite inclusions; the compositions vary from close to endmember diopside to K-bearing omphacite; the pyroxene in diamond P3 has a slight excess of Al over Na, which must be accommodated by a Ca-Eskola-type substitution. Of the three garnet inclusions, the CaO concentration ranges from 8.14 – 17.64 % (and up to 20.00 % in the estimated bulk composition in diamond P21), and two have a significant majorite component. In contrast, only a small variation was observed in the composition of ferropericlase, which was observed in five diamonds: on average they have Mg# = 87.0 ± 1.2 and contain 1.28 ± 0.10 % (1σ) NiO.

3.4 N concentrations and C isotopes

Nitrogen concentrations and aggregation states are given in Table 5. Nitrogen concentrations vary from < 3 – 1650 ppm, and the aggregation state varies from pure IaA to pure IaB. Sixteen (36 %) of the diamonds are classified as Type IIa, i.e. < 20 atomic ppm N, half of which have sublithospheric inclusions. Except for diamonds P6, P40 and P43, all the diamonds studied have the expected relationship between platelet content and the concentration of B-defects ("regular" in the terminology of Woods, 1986). Diamonds P16, P40, P42 and P43 were the only samples to have discrete variation in the concentration and/or aggregation state of N. Peridotitic diamond P16 (discussed in detail in Kohn et al., *this issue*) has three zones separated by sharp transitions: a Type IaB core (900 μm diameter) with a high concentration (500 – 1000 ppm) of N and an intense VN_3H peak at 3107 cm^{-1} (Goss et al., 2014), surrounded by a 200 μm wide zone of Type IIa diamond, and a narrow (<100 μm) rim of Type IaA diamond with ~ 360 ppm N. Representative spectra of these three zones are illustrated in Fig. 5a. Diamond P40 has 230 ppm N in its core (750 μm diameter), which is platelet degraded and has complex patchy CL zoning, and has an oscillatory-zoned Type IIa rim, and diamond P42 has a Type IaB core (1200 μm diameter) surrounded by a 150 μm wide less-aggregated rim. Diamond P43 has a N-poor and platelet-degraded core (1600 x 900 μm) surrounded by a 250 μm wide rim with a higher concentration of N and less platelet degradation; representative spectra of the core and rim are shown in Fig. 5b.

The carbon isotopic results from SHRIMP SI and the Cameca 1270 were within error of each other. However, calibration using diamond standard "synthetic A" ($\delta^{13}C_{PDB}$ = -23.9 ‰; Harte et al., 1999; also referred to as SYNAL e.g. Thomson et al., 2014) repeatedly yielded values that were ~ 0.4 ‰ lower than when using S0270 of Stern et al. (2014). For consistency with the extensive corpus of published data from EIMF, the values reported here (Table 6) are based on "synthetic A". The reproducibility of replicate measurements varied from 0.1 – 0.2 ‰, which we take to be the limit of accuracy of this technique. In the samples analysed, $\delta^{13}C_{PDB}$ ranges from -18.5 – -0.3 ‰, i.e. from values slightly heavier than typical peridotitic mantle diamond (-4 to -6 ‰) to light values typically associated with eclogitic diamonds (Cartigny et al., 2014). The isotopic compositions of the six lithospheric peridotitic diamonds are within the normal range for mantle carbon, with average values for each diamond ranging from -4.5 to -5.3 ‰. P14 and P16 have trends of $\delta^{13}C$ increasing core to rim; P7 and P40 are rather homogeneous and P9 has fluctuating $\delta^{13}C$ in the range -5.3 to -3.6 ‰. Only two unambiguously eclogitic diamonds, P3 and P17, were analysed. For both, $\delta^{13}C$ is < -10 ‰ and increases core to rim. P19, P31 and P44 are believed to be lithospheric because of their high N content and weak N aggregation; these are homogeneous and span the range of $\delta^{13}C$ = -2.8 to -7.6 ‰. The majority of the superdeep diamonds are isotopically homogeneous.

4. Discussion

4.1 Conditions of diamond formation

The external morphology of the ultradeep and lithospheric (eclogitic and peridotitic) diamonds is similar: dodecahedral diamond shapes predominate and the majority of the stones have features of wear and transportation. In contrast, the lithospheric and superdeep populations differ in their internal growth structures. The lithospheric diamonds show simple octahedral zonation (Fig. 3a) and are grown by a layer-by-layer mechanism under the conditions of a low degree of carbon supersaturation (Sunagawa, 1984). The sublithospheric, ultradeep diamonds show a lack of growth zonation but are suggestive of brecciation, healing and plastic deformation (Fig. 3b-d).

4.2 Composition of mineral inclusions

4.2.1 Olivine

The majority of the olivine inclusions in the Machado River diamonds are compositionally similar to those from lithospheric diamonds, being mostly highly magnesian and Ni-rich (Stachel and Harris, 2008; Sobolev et al., 2010). The less forsteritic olivines probably derived from a more fertile (lherzolitic) mantle lithology; the more forsteritic inclusions are suggestive of derivation from a harzburgitic or dunitic source, though lherzolitic olivines from the Mir kimberlite have unusually high Mg# (Stachel and Harris, 2008; Sobolev et al., 2009). The large range of olivine compositions at Machado River implies significant heterogeneity in the lithospheric mantle beneath the area. It is more typical to have small standard deviations for olivine inclusions within a region, e.g. a value of 0.9 for the Russian kimberlite fields of Alakit (four kimberlites) and Malo-Botuobiya (three kimberlites), as illustrated in Fig. 6. Similarly low standard deviations are observed in the alluvial diamond deposits in the Urals and north-eastern Siberia, both of which presumably derived from multiple kimberlites across a wide source area (Sobolev et al., 2009).

The olivine in diamond P33 is highly anomalous compared to typical lithospheric olivine inclusions in diamond (Stachel and Harris, 2008; Sobolev et al., 2009). Its elevated Al_2O_3 and CaO, and low Mg#, are indicative of wadsleyite or ringwoodite (Stachel, 2001), although Raman spectroscopy demonstrates this inclusion has retrogressed to the olivine structure. The low Ni (< 0.02 %) of this inclusion is intriguing. Brey et al. (2004) considered low Ni in olivine to be

indicative of equilibrium with ferropericlase, but the concentration observed here is too low to be explained by such an effect. Moreover, Fe-Mg partitioning between olivine and ferropericlase would require the latter to have an Mg# < 75 (Wiser and Wood, 1991), which is well outside the range observed at Machado River. Instead, it could be explained either by formation in a non-mantle Mg-rich lithology, or in a more reduced, deep region of the mantle where Ni has precipitated as metal and perhaps mechanically segregated (Frost and McCammon, 2008).

The olivine in diamond P20 forms part of a composite inclusion with orthopyroxene, and will be discussed in the following section.

4.2.2 Orthopyroxene

Two Machado River diamonds have compositions (particularly NiO content) typical of a lithospheric origin (Stachel and Harris, 2008). The orthopyroxene in diamond P37 (Mg# = 94.5) is typical of a peridotitic source (average Mg# = 94.2 ± 1.7; Stachel and Harris, 2008), whereas for the less magnesian orthopyroxene in sample P14 (Mg# = 86.9, in coexistence with an olivine of Mg# = 89.9, Fig. 6) a websteritic provenance (average Mg# = 84 ± 4; Stachel and Harris, 2008) is indicated.

The remainder of the orthopyroxene inclusions have < 0.05 % NiO and are therefore consistent with formation by retrogression of the lower mantle mineral bridgmanite (Stachel et al., 2000b). The cuspate margins of the composite olivine + orthopyroxene inclusion in diamond P20 (Fig. 3a) and the enstatite in P11are indicative of plastic deformation in the surrounding diamond, a feature that has been documented for inclusions undergoing a phase transformation during decompression (Cayzer et al., 2008; Zedgenizov et al., 2015). The volume change at the orthoenstatite/high-clinoenstatite phase transition (8 GPa) is only ~ 3% (Angel et al., 1992) and therefore unlikely to be responsible for the textures observed. The bulk composition of the inclusion in P20 does not correspond to a known mineral; however, we consider this to be a sampling artefact and that this inclusion is probably equivalent to the one shown in Fig. 6k of Hayman et al. (2005) where jeffbenite (formerly known as TAPP; Nestola et al., *in press*) was reported as a third mineral in the assemblage. Diamond P33 contains a composite inclusion of orthopyroxene + a mineral that is compositionally similar to jeffbenite (i.e. stoichiometry and lack of Ca); Raman spectroscopy did not confirm the presence of jeffbenite but did indicate the existence of unexposed forsterite within this composite inclusion.

Many of the lower mantle orthopyroxene inclusions (after bridgmanite) in the Machado River diamonds have very high Mg#, up to 97.0, and all have very low NiO contents, both of which are attributed to coexistence with ferropericlase (discussed in Section 3.5.x). The orthopyroxene inclusions in P11 and P15 appear to be single-phase, though further study is required to confirm the absence of exsolved phases below the polished surface. The five analysed in diamond P11 vary in composition: their Mg# and Al_2O_3 contents are weakly correlated, but the variation in CaO between these inclusions shows no relationship to the analysed elements and extend to both higher and lower concentrations than orthopyroxene inclusions in diamonds from Snap Lake, Canada (Pokhilenko et al., 2004). It is not clear whether the variations observed are primary, or whether they have been imposed by diffusion kinetics and/or varying pressures of retrogression, with exsolved components currently not visible at the surface. For example, the maximum possible concentrations of Al_2O_3 and CaO in “enstatite” *sensu lato* decrease with increasing pressure, particularly above 8 GPa and the orthoenstatite/high-clinoenstatite phase transition (Brey et al., 2008). The re-integrated bulk composition of former bridgmanite in P33 has ~ 3.8 % Al_2O_3, indicating that at least some of the source region for the Machado River superdeep diamonds contained aluminous bridgmanite. The trace element concentrations in the former

bridgmanite inclusions are low, as is the case for many in the Juina region (Harte et al., 1999), and are significantly lower than in lithospheric orthopyroxene at Machado River.

4.2.3 Ferropericlase

The compositional range of ferropericlase in Machado River diamonds is less than at other alluvial deposits and significantly higher in Mg# than the majority of inclusions in Juina-region superdeep diamonds (Fig. 7a; sources include Harte et al., 1999; Stachel et al., 2000b; Kaminsky et al., 2001; Hayman et al., 2005; Zedgenizov et al., 2014a). Ferropericlase with similar Mg# are common at Kankan, Guinea (Stachel et al., 2000b), Koffiefontein, South Africa (Harte et al., 1999) as well as other localities (see Thomson et al., 2016, for a compilation).

The marked enrichment of Ni in ferropericlase is attributed to a high partition coefficient $D_{\mathrm{Ni}}^{\mathrm{fper/bri}}$ (e.g. > 35, Malavergne et al., 1997). Coexisting orthopyroxene is even more depleted in Ni (apparent $D_{\mathrm{Ni}}^{\mathrm{fper/bri}} > 60$) than would be expected from experimental observations, both at Machado River and elsewhere (Harte et al., 1999) but, as noted above, the orthopyroxene is rather variable in composition and may have exsolved other phases that could account for the small Ni deficit; moreover the analysis of trace Ni in fine-grained experimental materials may have large errors. $K_{\mathrm{Fe\text{-}Mg}}^{\mathrm{fper/bri}}$ (= $(\mathrm{Fe/Mg})_{\mathrm{fper}}/(\mathrm{Fe/Mg})_{\mathrm{bri}}$) has been shown experimentally to be 3 – 6 in Al-free lithologies and decreasing to ~ 1 when the bridgmanite contains 4 % Al_2O_3 (Wood, 2000), which is in good agreement with the behaviour observed in P11 ($K_{\mathrm{Fe\text{-}Mg}}^{\mathrm{fper/bri}} = 3.7$, Al_2O_3 = 0.24 ± 0.08 %) in P11 and in P15 ($K_{\mathrm{Fe\text{-}Mg}}^{\mathrm{fper/bri}} = 2.9$, Al_2O_3 = 1.02 %). With the exception of Mn, Co and Na, all other trace elements occur at extremely low concentrations in ferropericlase.

4.2.4 Garnet

The apparent minor majorite component in garnet in diamond P24 (3.05 Si on a 12 O basis) is attributed to an analytical artefact (a low total, 97.2 %), and a lithospheric eclogitic source is inferred from the low Mg# and high Ca content of this garnet. True majoritic garnet was observed in two diamonds, P21 and P23. The high Mg# of these two majoritic garnets (86.9 and 89.5 respectively) is unusual compared to other superdeep diamond occurrences (Fig. 7b), in which highly magnesian majoritic garnet (Mg# > 80) generally has > 1 % Cr_2O_3, as at Snap Lake, Canada (Pokhilenko et al., 2004) and at Pipe 50, China (Wang et al., 2000).

The majorite garnet in diamond P21 has retrogressed to diopside + non-majoritic calcic pyrope, with an estimated bulk composition containing 3.34 Si per formula unit (pfu, calculated to 12 O). This inclusion is notable for having a higher CaO content than any previously reported majorite (Kiseeva et al., 2013). Although the Si content has been used extensively as a barometer (e.g. Stachel, 2001), Collerson et al. (2010) noted that the effect of Ca was poorly constrained and excluded $CaSiO_3$-bearing assemblages from their calibrations; therefore we do not estimate a pressure of formation for this sample. The trace element concentrations in this garnet (Fig. 7c) are very similar to those reported from high-Ca majoritic garnets from Kankan, Guinea (Stachel et al., 2000a), and to the most enriched majoritic garnets from São Luiz, Brazil (Harte, 2010).

A homogeneous majoritic garnet, i.e. lacking exsolved diopside, was observed in diamond P23; at 3.44 Si pfu this is one of the highest majorite contents of any reported garnet, with only two diamond inclusions from Jagersfontein having a greater Si excess (Fig. 7b). The composition of this garnet is similar to one synthesised experimentally from a pyrolitic bulk composition at 14.6 GPa by Akaogi and Akimoto (1979), which had Mg# = 82.2 and Si = 3.30 pfu. It seems likely

the inclusion in diamond P23 formed at pressures significantly in excess of 15 GPa (i.e. depths > 440 km; Dziewonski and Anderson, 1981), in light of its high majorite content.

4.2.5 Clinopyroxene

The clinopyroxene inclusions in diamonds P27 and P29 are typical in composition for diamondiferous eclogites (Stachel and Harris, 2008). The inclusion in diamond P3 is more unusual; its Ca-Eskola component (~ 11 % of the pyroxene composition) implies some combination of lower pressures, higher temperatures and higher silica activities (Knapp et al., 2013), i.e. a lithospheric origin. This pyroxene may derive from a metasomatic lithology (pyroxenite *sensu lato*) intermediate between eclogite and websterite, on account of its higher Mg# (89.6), Cr and Ni content compared to the other two omphacites (Mg# = 73.1 and 77.9 in P27 and P29 respectively), and LREE enrichment compared to average omphacite inclusions (Stachel et al., 2004).

Diopside is present in diamond P11. Several features (inclusions of ferropericlase and low-Ni orthopyroxene, plastic deformation around several inclusions, < 2 ppm N in the diamond) strongly suggest a lower mantle origin for this diamond, which represents a paradox because diopside is not stable above ~ 16 GPa (Gasparik, 1996). It is possible that this diopside represents the only visible phase of a composite inclusion, e.g. an exsolution from a former Ca-bearing bridgmanite. Diopside is also present in composite former majorite garnet (see above) and in former $CaSiO_3$-perovksite (see below).

4.2.6 Carbonates

Diamonds P15 and P21 contain inclusions that are inferred, because of low EPMA totals, low SiO_2 and high Ca concentrations and lack of other elements identified by EDS, to be carbonates of dolomitic composition, though the small size of the inclusions has partially compromised the analyses. Both diamonds are considered to be superdeep on the basis of other inclusions present in these diamonds. Raman spectroscopic observation of diamond P33 allowed an unexposed inclusion to be identified as dolomite, and revealed the presence of magnesite (apparently not exposed at the surface) within the olivine inclusion. Carbonate inclusions have been observed in other Brazilian superdeep deposits, e.g. Collier-4 (Bulanova et al, 2010; Burnham et al., 2015), Juina-5 (Thomson et al., 2014a) and the Rio Soriso and São Luiz alluvial deposits (Kaminsky et al., 2013; Zedgenizov et al., 2014 a, b), and are strong evidence for the involvement of a slab-derived carbonate melt in the formation of the superdeep diamonds at those localities (Thomson et al., 2014a; Thomson et al., 2016).

4.2.7 Former $CaSiO_3$-perovskite

Composite inclusions of Ca-walstromite + diopside were exposed in diamonds P4 and P28; the latter is illustrated in Fig. 4b. Diamond P4 also contained an inclusion of merwinite + diopside. The simplest explanation is that these inclusions originally existed as single phase $CaSiO_3$-perovskite grains that have subsequently retrogressed to Ca-Mg silicate assemblages. Merwinite ($Ca_3MgSi_2O_8$) has previously only once been reported as an inclusion in a diamond (Zedgenizov et al., 2014b). Its (Ca+Mg)/Si ratio is higher than that of $CaSiO_3$; we interpret this as analogous to the retrogression of former $CaSiO_3$-perovskite inclusions in diamonds from Kankan, Guinea, where some inclusions are single-phase Ca-walstromite but others consist of larnite (Ca_2SiO_4) + $CaSi_2O_5$-titanite + $CaSiO_3$ (Joswig et al., 1999). The phase diagram for $CaSiO_3$ implies that Ca-walstromite and Ca_2SiO_4 + $CaSi_2O_5$ represent retrogression at lower (~ 3 – 10 GPa) and higher pressures (~ 10 – 12 GPa) respectively (Gasparik et al., 1994). Merwinite presumably occurs in preference to larnite in more magnesian systems, and the coexistence within a single diamond of two different sets of daughter phases cannot be explained by different pressures of re-

equilibration. Additional factors such as the presence of suitable surface defects to promote heterogeneous nucleation probably play a role in controlling retrogression of inclusions in superdeep diamonds. Such kinetic limitations make it unlikely that the superdeep diamonds experienced a long period of shallower storage prior to eruption.

The former $CaSiO_3$-perovskites in Machado River diamonds are rare exceptions to the common tendency for inclusions of this mineral to have Mg contents well below the concentration expected for coexistence with bridgmanite (Armstrong et al., 2012; Thomson et al., 2016). In the Juina-5 and Collier-4 superdeep diamonds it is more typical for the $CaSiO_3$-perovskite to have exsolved $CaTiO_3$ and occasionally also ZrO_2, and other high field strength elements such as Nb and Hf are significantly higher in the Collier-4 and Juina-5 $Ca(Si,Ti)O_3$ inclusions (Bulanova et al., 2010; Thomson et al., 2014a; Burnham et al., 2015). At Collier-4 and at Machado River, this mineral is enriched in the light (L) REE relative to the heavy REE; however, the $CaSiO_3$ analysed in the present study (Tables 3 and 4) have all REE concentrations lower by one to two orders of magnitude (Fig. 7d), and the concentration of Rb is at least two orders of magnitude lower.

Anzolini et al. (this issue) observed the residual pressure on single-phase $CaSiO_3$ inclusions in diamond to be much lower than expected on the basis of the unit cell volumes of $CaSiO_3$-perovskite, Ca-walstromite and the thermoelastic properties of those phases; moreover, they considered 30% plastic deformation of the host diamond to be implausibly large for the samples of their study. This interpretation does not agree with observations of Ca-walstromite inclusions from Machado River, Collier-4 and Juina-5. In diamonds from these localities, inclusions of this mineral are generally polyphase, which is indicative of formation as $(Ca,Mg)SiO_3$ perovskite at Machado River and $Ca(Si,Ti)O_3$ perovskite at Collier-4 and Juina-5 (e.g. Bulanova et al., 2010; Walter et al., 2011; Thomson et al., 2014; Burnham et al., 2015). In addition to the compositional data there is textural evidence for extreme deformation around these inclusions: curved, irregular and often concave interfaces with the diamond, and tapering cracks that radiate away from the inclusion and are infilled with Ca-walstromite. Zedgenizov et al. (2015) observed significant distortion of the diamond lattice around $CaSiO_3$ inclusions, as well as around other minerals believed to have undergone phase transitions. Although Anzolini et al. are correct to point out the possibility of primary Ca-walstromite inclusions in diamonds, the conclusion we draw is that it is possible for this mineral to form retrogressively without retaining large internal pressures and that the large volume change must consequently be accommodated by a combination of plastic and brittle deformation, as demonstrated by electron back scatter diffraction (Zedgenizov et al., 2015) and cracking (Bulanova et al., 2010; Thomson et al., 2014; Burnham et al., 2015) respectively.

4.2.8 Sulphides

Sulphides were located in six diamonds; their Ni and Cr concentrations, some of which are reported in Table 2, indicate peridotitic affinities for P5 and eclogitic affinities for P6 P8, P10, P17 and P27 (Stachel and Harris, 2008).

4.2.9 Other inclusions

The inclusions with K-feldspar-like compositions in P2 could represent retrogressed K-hollandite (e.g. Plá Cid et al., 2014) but may be epigenetic. SiO_2 (polymorph not determined) was located in P23 and P34 and is assigned to the eclogitic superdeep paragenesis on the basis of the other inclusions in those samples.

4.3 Nitrogen concentrations and aggregation states

Although many lithospheric diamonds are Type IIa, the majority are Type I and have measurable N concentrations. Contrastingly, almost all superdeep diamonds have low concentrations of N (e.g. Hutchison et al., 1999), though exceptionally Burnham et al. (2015) reported one superdeep diamond (ColN-15, from Juina-region pipe Collier-4) containing 450 ppm N. These observations are true of the Machado River diamonds: all samples that are considered superdeep on the basis of their inclusions have < 50 ppm N. Where N is present in superdeep diamonds, it is generally fully aggregated, and the platelet peak is of low intensity or absent (Kaminsky et al., 2001; Thomson et al., 2014a). A decreased platelet peak area, referred to as "degraded" or "irregular", suggests high temperature storage and/or plastic deformation to convert the platelets (interstitial C) into dislocation loops (Woods, 1986; Evans et al., 1995), both of which are conditions likely to be experienced in the asthenosphere and lower mantle. The platelet degradation observed in the core of diamond P40, coupled with the CL textures, may suggest that the core of diamond P40 is superdeep in origin, though core and rim have C isotopic compositions within error. Platelet degradation is also evident in P43, which has a low-N core (34 ppm) that completely lacks platelets, overgrown by a rim with much higher N (310 ppm) in which the area of the platelet peak is only ~ 30 % of what would be expected. Similarly, the core of P43 has CL characteristics that suggest it is superdeep, especially the patchy, irregular and polycentric nature of the zonation (Fig. 3d); the rim, with characteristics reminiscent of lithospheric diamonds (higher N, sharp oscillatory zoning, less platelet degradation) may have grown during the convective ascent of the superdeep material.

Combining C isotopic data with FTIR data suggests strong similarities between the histories of P16 and P42: both have cores with $\delta^{13}C$ = -6.1 ‰ overgrown by discrete younger (Type IaA) rims with $\delta^{13}C$ = -4.8 ‰ (allowing for the ~ 0.1 ‰ uncertainty in the measurements).

When the concentrations and aggregation states for the diamonds are considered, the diamonds cover a wide range of model temperatures, as demonstrated in Fig. 8 (approximately 1050 – 1250 °C when using a 1.5 Ga mantle residence time, following Hunt et al., 2009), indicating either diamond formation over a range of temperatures (and hence presumably depths) or multiple episodes of diamond formation. The overgrowths in diamonds P16 and P42 are clear textural and spectroscopic evidence for the latter hypothesis, but it is not possible to determine whether the entirely Type IaA stones relate to the younger growth events or are older diamonds that have remained unaggregated because of storage conditions that were up to 200 °C cooler than the Type IaB stones. The presence of multiple discrete growth events in some diamonds is an important reminder of the importance of *in situ* examination of inclusions and their relationship to CL and FTIR zonation (Bulanova, 1995).

4.4 Carbon isotopes

The core-to-rim zonation observed in the lithospheric diamonds is consistent with diamond crystallisation from an oxidised (CO_2/carbonate) fluid (Deines, 1980).

The isotopic composition of the superdeep diamonds (including those defined as superdeep solely on the basis of low N concentrations and platelet degradation) at Machado River is predominantly heavy (22 % have $\delta^{13}C$ > -3.5 ‰). In contrast, most other Brazilian superdeep diamond suites have $\delta^{13}C$ << -3.5 ‰, as summarised in Fig. 9. Only 8 % of 252 alluvial diamonds in the Juina region (Hutchison et al., 1999; Kaminsky et al., 2001, 2009; Zedgenizov et al., 2014a) have $\delta^{13}C$ > -3.5 ‰. Isotopically heavy diamonds are generally rare, with the alluvial deposits of south-east Australia accounting for the majority of samples worldwide (Cartigny et al., 2014), but may be locally common as at Machado River and at Kankan, Guinea (Stachel et al., 2002). Values of $\delta^{13}C$ > -3.5 ‰ are characteristic of marine carbonates, both

hydrothermal and sedimentary (Hudson, 1977; Alt and Teagle, 2003). The aspects of the carbon cycle that result in such a scarcity of diamonds with isotopically heavy carbon remain elusive.

Carbon isotope variations in a single diamond may be due to isotopic fractionation or mixing between two carbon sources. At the high temperatures of superdeep diamond formation the fractionation between fluid and melt would be expected to be low, but mixing has been demonstrated to be an important factor in other superdeep diamond suites (Burnham et al. 2015). Therefore the homogeneity observed in the Machado River diamonds, coupled with diffuse zoning textures, may indicate that they were stored at sufficiently high temperatures for diffusion to occur. The spatial distribution of CL intensity in diamond P30 was assessed using the software *ImageJ*, with a wide line to average out noise in the data. For this exercise, and indeed any attempt to interpret suspected diffusion profiles, it is preferable to have a simple (i.e. plane-parallel) geometry, a lack of cross-cutting features (e.g. "wrinkles" and cracks) and adjacent wide homogeneous zones that allow the boundary conditions of the diffusion profile to be inferred. There are two such regions within this diamond (Fig. 10a). The profile of the CL intensity across these boundaries can be modelled as an error function (Equation 52 of Zhang, 2010), i.e. the shape expected for diffusive relaxation of a step function (Fig. 10b). The similarity of these length scales in the two profiles (which indicates that profile B would have taken 2.8 times as long as Profile A to form, though it is possible B was initially a less sharp profile), the excellent fit of the diffusion equation and the opposite polarities of the profiles (dark to light in profile A, light to dark in profile B) are consistent with the hypothesis that the diffuse features are diffusion related, rather than coincidences of the growth behaviour. Estimating time scales for diffusion in these samples is not possible for three reasons. 1) The cause of the CL in this sample is not known: N, a major luminescence activator, is below the limit of detection; 2) it is not known whether plastic deformation could have accelerated diffusion, and 3) the storage temperature for this diamond is unconstrained. However, as an illustrative example, we note that if the luminescence activator diffused at the same rate as C, the observed profiles would be generated in 4.5 – 12 Ma at 1400 °C or 87-240 Ma at 1300 °C (Koga et al., 2005).

4.5 A model for the formation of the Machado River superdeep diamonds

For the majority of the superdeep diamonds in the Juina region of Brazil, especially those found in the Collier-4 and Juina-5 kimberlites, it has been demonstrated that they are not derived from pure eclogitic or peridotitic source regions; instead, the formation of the diamonds and their inclusions is best explained by metasomatic reaction of a slab-derived alkali-rich carbonatite melt with ambient reduced mantle (Walter et al., 2008; Bulanova et al., 2010; Walter et al., 2011; Burnham et al., 2015; Thomson et al., 2016; Thomson et al., *this issue*). The Machado River superdeep diamonds are markedly different from the Juina-region samples, and indeed from many other superdeep diamond localities in several respects:

(1) The inclusions in Machado River diamonds tend to have higher Mg# and lower trace element concentrations (e.g. Fig. 7). One exception is that majorite in diamond P21 has high REE concentrations that are similar to those in majorite at Kankan, Guinea.

(2) Several inclusions in Machado River diamonds are highly calcic, e.g. the garnet in diamond P21 and the dolomite inclusions, which contrast with the ferroan magnesite observed at Collier-4 and Juina-5 (Thomson et al., 2014; Burnham et al., 2015).

(3) Many of the Machado River diamonds are composed of isotopically heavy carbon, in contrast to the light carbon at Collier-4 and Juina-5 and the mantle-like carbon in many of the Juina-region alluvial diamonds (Fig. 9).

A model for superdeep diamond formation at Machado River must explain the above observations and take into account the evidence for the involvement of crustal components in the

548 Machado River source region: the $CaSiO_3$ inclusion in diamond P28 has an oxygen isotopic
549 composition of $\delta^{18}O = 7.6$ ‰ (Burnham et al., 2015). We propose that diamond formation in the
550 Machado River superdeep source is likely to have proceeded by a reaction between a carbonate-
551 bearing slab-derived fluid component and the ambient mantle, by analogy to Juina-5 and Collier-
552 4. It is not possible to constrain the identity of the subducted component(s) uniquely. The
553 magnesian compositions of the inclusions suggest, however, that either the mantle component
554 predominated, or the crustal component was itself highly magnesian, or both. For example, as
555 noted above, the composition of garnet in diamond P23 is similar to one produced
556 experimentally from fertile peridotite at pressures equivalent to 430 km depth (Akaogi and
557 Akimoto, 1979), except for a higher majorite component (which would require deeper
558 formation) and higher Mg#. The latter cannot be explained by formation from a more depleted
559 peridotite, as this would result in a higher concentration of Cr, and some other source of Mg-
560 enrichment must be involved.
561
562 The calcium-rich inclusions and heavy carbon isotopic compositions of the diamonds are both
563 consistent with contributions from carbonates, either seawater-derived hydrothermal calcite or
564 sedimentary limestone. These lithologies are both depleted in trace elements, with the latter
565 having low REE, Zr, Nb, Ti and Rb, among other elements, compared to shales and basalts
566 (Turekian and Wedepohl, 1961), and with vein calcites containing only ppb-level concentrations
567 of REE (Bach et al., 2011).
568
569 At 20 GPa, melting begins at 1640 °C in the system $MgCO_3$-$CaCO_3$ (Thomson et al., 2014b),
570 but at this pressure the slab temperature is probably in the range 1000 – 1300 °C (Peacock, 1990;
571 Fukao et al., 2009), which would seem to preclude melting of Na-poor carbonates. Water is
572 known to reduce the melting temperature of carbonates dramatically at lower pressures (Lentz,
573 1999), and as water appears to play a significant role in the formation of some superdeep
574 diamonds (Pearson et al., 2014) it seems reasonable to believe it may have facilitated the fluid-
575 mediated transport of Ca- (and possibly Mg-) bearing carbonates here. Meta-serpentinite is a
576 conveniently trace-element-poor and magnesium-rich source of water (e.g. Li et al., 2004), with
577 the water primarily held in wadsleyite, ringwoodite and superhydrous phase B at Transition
578 Zone pressures (Ohtani et al., 2004; Komabayashi and Omori, 2006; Harte, 2010).
579
580 At low pressures (< 5 GPa) two slab-derived fluids are possible: aqueous fluids, which have only
581 a limited capacity for transporting major and trace elements, and hydrous silicate melts, which
582 can mobilise orders of magnitude higher concentrations of most elements (Hermann et al.,
583 2013). At higher pressures, including those relevant to the formation for the superdeep
584 diamonds, there is a continuum between aqueous fluid and carbonate- and/or silicate-rich melt
585 (e.g. Mibe et al., 2004) and therefore the transport capacity of this fluid depends strongly on
586 temperature, with low solute concentrations in low-temperature aqueous fluids, and high
587 concentrations in hydrous melts. A fluid on this spectrum would allow slow percolation of slab
588 material into the surrounding mantle.
589
590 Is it possible that the trace-element-poor subducted lithology is in fact the residue of basaltic
591 material after extraction of the trace-element-enriched carbonate melt that gave rise to the Juina-
592 5 and Collier-4 diamonds? It seems improbable because of the contrast in C isotope signatures
593 between the Machado River and the Juina-region diamonds; migration of the melt seems likely
594 to have homogenised the C reservoirs in the slab. Moreover, such a residue would be greatly
595 depleted in the LREE, which are enriched in the $CaSiO_3$ inclusion in P28.
596

In the absence of experimental data on the melting of hydrous carbonated lithologies at Transition Zone and lower mantle pressures, it is not clear what combination of water (as a fluxing agent), peridotite and serpentinite (as sources of Mg, with serpentinite often having higher Mg# than peridotite, e.g. Li et al., 2004) and carbonate (as a fluxing agent and a source of C, Ca and/or Mg) are necessary to provide the observed inclusion assemblages. The compositional constraints, alongside the physical challenge of generating a carbonate-bearing diamond-forming fluid at the expected temperatures of a subducted slab in the Transition Zone and lower mantle, seem to leave no obvious alternative models.

4.6 Possible primary sources of the Machado River alluvial diamonds

The Machado River population consists of ~ 50 % lithospheric (16 % peridotitic, 11 % eclogitic, 22 % uncertain paragenesis), ~ 30% sublithospheric diamonds and ~ 20 % Type IIa diamonds of unknown paragenesis, as summarised in Fig. 11 and Table 5. The variety of mineral inclusions and surface features on the diamonds, outlined above, suggest multiple kimberlitic sources, though both lithospheric and superdeep diamonds have been recorded together in individual pipes such as those at Diavik in Canada (Davies et al., 1999) and Jagersfontein, South Africa (Deines et al., 1991).

Surface abrasion features on the majority of Machado diamonds are consistent with extensive alluvial re-working. The presence of frequent brown as well as green radiation spots implies heating during burial (Vance and Milledge, 1972), most likely in a sedimentary collector such as the basal Cretaceous Parecis Formation conglomerates (Fig. 1b, c). The minor population of unworn octahedral stones may, in contrast, have been derived directly from local kimberlites without extensive sedimentary reworking. The Araras kimberlites (Fig. 1b) just upstream of the Machado River alluvials are barren of diamonds. The presence further upstream of the diamondiferous Triassic-aged Carolina and Pimenta Bueno kimberlite pipes could suggest that these pipes have supplied some of the diamonds for the Machado River alluvials. However, the Carolina kimberlite (Fig. 1b) is unlikely to have supplied a significant proportion of the Machado River diamonds because platelet degradation is seen in a large proportion of Carolina diamonds (Hunt et al., 2009), a feature uncommon at Machado. The Pimenta Bueno kimberlites have not yielded significant numbers of commercial-sized diamonds and hence are not a major supplier to Machado either. The ultimate sources may well include kimberlites in the Roosevelt Reserve or even still buried beneath Cretaceous sediments further south. Alluvial deposits on the Roosevelt Reserve contain a significant (~ 25 %) proportion of diamonds with N < 100 ppm, many of which have experienced platelet degradation (Borges, 2009), and although the inclusions have not been studied it seems likely that this population of diamonds is the same as, or related to, the superdeep suite at Machado River.

5. Conclusions

Multiple kimberlite sources are envisaged for the Machado River diamonds. On the basis of inclusion mineralogy and chemistry, FTIR characteristics and carbon isotope compositions there are at least two discrete populations: a lithospheric suite comprising peridotitic and eclogitic lithologies, and a superdeep suite comprising ferropericlase, majoritic garnet, bridgmanite, $CaSiO_3$-perovskite and ringwoodite (prior to retrogression). Notable wear features and radiation damage on the stones suggest recycling from burial in sediments, with potential additional kimberlite sources in the Roosevelt Reserve or beneath Cretaceous sediments further south.

The lithospheric mantle is heterogeneous in the region below the Machado River primary source region, with lherzolitic and harzburgitic peridotites (indicated by the range of olivine compositions), eclogite and intermediate lithologies (omphacite in P3). The heterogeneity may

be both lateral and vertical if there is more than one source for the lithospheric diamonds at Machado River. The region has also experienced more than one episode of diamond formation (evinced by Type IaA rims on older diamonds).

The presence of carbonate inclusions in three samples suggests that the superdeep suite of diamonds formed by reaction of slab-derived carbonate-bearing fluid or carbonatitic melt with reduced ambient mantle, as at other superdeep localities in Brazil (Bulanova et al., 2010; Thomson et al., 2014a; Burnham et al., 2015; Thomson et al., 2016). However, the subducted component shows some marked differences from that in the Collier-4 and Juina-5 superdeep diamonds: on the basis of carbon isotopes and inclusion chemistry the latter two seem likely to derive from a mixture of altered sea-floor basalts and shales, whereas the Machado River superdeep diamonds are more likely to relate primarily to subducted carbonates (sedimentary limestones or vein carbonates) and serpentinites with only minor contributions from other lithologies, resulting in a suite of diamonds with heavy C isotope compositions and Mg- and Ca-rich inclusions. Collier-4 and Juina-5 diamonds probably formed predominantly at Transition Zone depths, whereas the Machado River superdeep assemblage has a large proportion of lower mantle diamonds. The preservation of compositionally (and isotopically) distinct units to such great depths further highlights the complexity of recycling crustal components back into the mantle (c.f. Harte, 2010; Burnham et al., 2015).

Acknowledgements

This project would not have been possible without extensive analytical support, and we gratefully acknowledge the contributions of Ben Buse and Stuart Kearns (SEM and EPMA at the University of Bristol), John Craven and Richard Hinton (SIMS at EIMF), Jeremy Wykes (LA-ICP-MS at the Australian National University) and Janaina Avila (SHRIMP at the Australian National University). Diamond standards were kindly supplied by Dan Howell and Tatsuo Irifune. We also thank Andy Thomson for additional C isotope measurements, David Fisher for sharing caxbd97.xls, Rio Tinto for samples and acknowledge support from the Natural Environment Research Council (grant NE/J008583/1 and EIMF awards IMF438/0511 and IMF512/2013. We are grateful to Dmitri Zedgenizov and Ben Harte for their careful and helpful reviews of the manuscript, and to Fabrizio Nestola for conceiving and successfully executing this special issue of *Lithos*.

References

Afanasiev, V.P., Yefimova, E.S., Zinchuk, N.N., Koptil, V.I., 2000. Atlas of morphology of diamonds from Russian sources. Russian Academy of Sciences, Siberian Branch, Novosibirsk, 291 pp.

Alt, J.C., Teagle, D.A.H., 2003. Hydrothermal alteration of upper oceanic crust formed at a fast-spreading ridge: mineral, chemical, and isotopic evidence from ODP site 801. Chemical Geology 201, 191-211.

Anzolini, C., Angel, R.J., Merlini, M., Derzsi, M., Tókar, K., Milani, S., Krebs, M.Y., Brenker, F.E., Nestola, F., Harris, J.W., *in press*. Depth of formation of $CaSiO_3$-walstromite included in super-deep diamonds. Lithos, this issue.

Armstrong, L.S., Walter, M.J., Tuff, J.R., Lord, O.T., Lennie, A.R., Kleppe, A.K., Clark, S.M., 2012. Perovskite phase relations in the system CaO-MgO-TiO_2-SiO_2 and implications for deep mantle lithologies. Journal of Petrology 53, 611-635.

Bach, W., Rosner, M., Jons, N., Rausch, S., Robinson, L., Paulick, H., Erzinger, J., 2011. Carbonate veins trace seawater circulation during exhumation and uplift of mantle rock: Results from ODP Leg 209. Earth and Planetary Science Letters 311, 242-252.

696 Borges, M.P.A.C., 2009. Mineralogia dos diamantes da terra indígena Roosevelt – RO. Masters
697 dissertation, University of Brasilia.
698 Brey, G.P., Bulatov, V., Girnis, A., Harris, J.W., Stachel, T., 2004. Ferropericlase—a lower
699 mantle phase in the upper mantle. Lithos 77, 655-663.
700 Bulanova, G.P., 1995. The formation of diamond. Journal of Geochemical Exploration 53, 1-23.
701 Bulanova, G.P., Smith, C.B., Kohn, S.C., Walter, M.J., Gobbo, L., Kearns, S., 2008. Machado
702 River, Brazil – a newly recognised ultradeep diamond occurrence. 9th International Kimberlite
703 Conference Extended Abstract No. 9IKC-A-00233.
704 Bulanova, G.P., Walter, M.J., Smith, C.B., Kohn, S.C., Armstrong, L.S., Blundy, J., Gobbo, L.,
705 2010. Mineral inclusions in sublithospheric diamonds from Collier 4 kimberlite pipe, Juina,
706 Brazil: subducted protoliths, carbonated melts and primary kimberlite magmatism.
707 Contributions to Mineralogy and Petrology 160, 489-510.
708 Burnham, A.D., Thomson, A.R., Bulanova, G.P., Kohn, S.C., Smith, C.B., Walter, M.J., 2015.
709 Stable isotope evidence for crustal recycling as recorded by superdeep diamonds. Earth and
710 Planetary Science Letters 432, 374-380.
711 Cartigny, P., Palot, M., Thomassot, E., Harris, J.W., 2014. Diamond formation: a stable isotope
712 perspective. Annual Review of Earth and Planetary Sciences 42, 699-732.
713 Cayzer, N.J., Odake, S., Harte, B. and Kagi, H., 2008. Plastic deformation of lower mantle
714 diamonds by inclusion phase transformations. European Journal of Mineralogy 20, 333-339.
715 Collerson, K.D., Williams, Q., Kamber, B.S., Omori, S., Arai, H., Ohtani, E., 2010. Majoritic
716 garnet: a new approach to pressure estimation of shock events in meteorites and the
717 encapsulation of sublithospheric inclusions in diamond. Geochimica et Cosmochimica Acta 74,
718 5939-5957.
719 Davies, R.M., Griffin, W.L., Pearson, N.J., Andrew, A.S., Doyle, B.J., O'Reilly, S.Y., 1999.
720 Diamonds from the deep, pipe DO-27, Slave Craton, Canada, in Gurney, J.J., Gurney, J.L.,
721 Pascoe, M.D., Richardson, S.H. (Eds.), Proceedings of the VIIath International Kimberlite
722 Conference, The J.B. Dawson Volume, Red Roof Design, Cape Town, 148-155.
723 Deines P. 1980. The carbon isotopic composition of diamonds: relationship to diamond shape,
724 color, occurrence, and vapor composition. Geochimica et Cosmochimica Acta 44, 943-961.
725 Deines, P., Harris, J.W., Gurney, J.J., 1991. The carbon isotopic composition and nitrogen
726 content of lithospheric and asthenospheric diamonds from the Jagersfontein and Koffiefontein
727 kimberlite, South Africa. Geochimica et Cosmochimica Acta 55, 2615-2625.
728 Dziewonski, A.M., Anderson, D.L., 1981. Preliminary reference Earth model. Physics of the
729 Earth and Planetary Interiors 25, 297-356.
730 Evans, T., Kiflawi, I., Luyten, W., Van Tendeloo, G., Woods, G. S., 1995. Conversion of
731 platelets into dislocation loops and voidite formation in Type IaB diamonds. Proceedings of the
732 Royal Society of London A 449, 295-313.
733 Frost, D.J., McCammon, C.A., 2008. The redox state of the Earth's mantle. Annual Review of
734 Earth and Planetary Sciences 36, 389-420.
735 Gasparik, T., 1996. Melting experiments on the enstatite-diopside join at 70–224 kbar, including
736 the melting of diopside. Contributions to Mineralogy and Petrology 124, 139-153.
737 Gasparik, T., Wolf, K., Smith, C.M., 1994. Experimental determination of phase relations in the
738 $CaSiO_3$ system from 8 to 15 GPa. American Mineralogist 79, 1219-1222.
739 Ghosh, S., Ohtani, E., Litasov, K.D., Terasaki, H., 2009. Solidus of carbonated peridotite from
740 10 to 20 GPa and origin of magnesiocarbonatite melt in the Earth's deep mantle. Chemical
741 Geology 262, 17-28.
742 Goss, J.P., Briddon, P.R., Hill, V., Jones, R., Rayson, M.J., 2014. Identification of the structure
743 of the 3107 cm^{-1} H-related defect in diamond. Journal of Physics: Condensed Matter 26,
744 145801.

745 Harte, B., 2010. Diamond formation in the deep mantle: the record of mineral inclusions and
746 their distribution in relation to mantle dehydration zones. Mineralogical Magazine 74, 189-215.
747 Harte, B., Fitzsimons, I.C.W., Harris, J.W. and Otter, M.L., 1999. Carbon isotope ratios and
748 nitrogen abundances in relation to cathodoluminescence characteristics for some diamonds
749 from the Kaapvaal Province, S. Africa. Mineralogical Magazine 63, 829-856.
750 Harte, B., Harris, J.W., Hutchison, M.T., Watt, G.R., Wilding, M.C., 1999. Lower mantle
751 mineral associations from São Luiz, Brazil. In: Fei, Y., Bertka, C.M.,Mysen, B.O. (Eds.),
752 Mantle Petrology: Field Observations and High Pressure Experimentation: A Tribute to Francis
753 R. (Joe) Boyd. Geochemical Society, pp. 125-153.
754 Harte, B., Richardson, S., 2012. Mineral inclusions in diamonds track the evolution of a
755 Mesozoic subducted slab beneath West Gondwanaland. Gondwana Research 21, 236-245.
756 Hayman, P.C., Kopylova, M.G., Kaminsky, F.V., 2005. Lower mantle diamonds from Rio
757 Soriso (Juina area, Mato Grosso, Brazil). Contributions to Mineralogy and Petrology 149, 430-
758 445.
759 Hermann, J., Zheng, Y.-F., Rubatto, D., 2013. Deep fluids in subducted continental crust.
760 Elements 9, 281-287.
761 Hudson, J.D., 1977. Stable isotopes and limestone lithification. Journal of the Geological
762 Society 133, 637-660.
763 Hunt, L., Stachel, T., Morton, R., Grütter, H., Creaser, R.A., 2009. The Carolina kimberlite,
764 Brazil — Insights into an unconventional diamond deposit. Lithos 112S, 843-851.
765 Hutchison, M., Cartigny, P., Harris, J.W., 1999. Carbon and nitrogen compositions and physical
766 characteristics of transition zone and lower mantle diamonds from Sao Luiz, Brazil, in:
767 Gurney, J.J., Gurney, J.L., Pascoe, M.D., Richardson, S.H., (Eds.), Proceedings of the 7th
768 International Kimberlite Conference. Red Roof Design, Cape Town, pp. 372-382.
769 Joswig, W., Stachel, T., Harris, J.W., Baur, W.H., Brey, G.P., 1999. New Ca-silicate inclusions
770 in diamonds – tracers from the lower mantle. Earth and Planetary Science Letters 173, 1-6.
771 Kaminsky, F.V., Zakharchenko, O.D., Davies, R., Griffin, W.L., Khachatryan-Blinova, G.K.,
772 Shiryaev, A.A., 2001. Superdeep diamonds from the Juina area, Mato Grosso State. Brazil.
773 Contributions to Mineralogy and Petrology 140, 734-753.
774 Kaminsky, F.V., Khachatryan, G.K., Andreazza, P., Araujo, D., Griffin, W.L., 2009. Super-deep
775 diamonds from kimberlites in the Juina area, Mato Grosso State, Brazil. Lithos 112S, 833-842.
776 Kaminsky, F.V., Wirth, R., Schreiber, A., 2013. Carbonatitic inclusions in deep mantle
777 diamonds from Juina, Brazil: new minerals in the carbonate-halide association. The Canadian
778 Mineralogist 51, 669-688.
779 Kiseeva, E.S., Yaxley, G.M., Stepanov, A.S., Tkalčić, H., Litasov, K.D., Kamenetsky, V.S.,
780 2013. Metapyroxenite in the mantle transition zone revealed from majorite inclusions in
781 diamonds. Geology 41, 883-886.
782 Knapp, N., Woodland, A.B., Klimm, K., 2013. Experimental constraints in the CMAS system on
783 the Ca-Eskola content of eclogitic clinopyroxene. European Journal of Mineralogy 25, 579-
784 596.
785 Koga, K.T., Van Orman, J.A., Walter, M.J., 2003. Diffusive relaxation of carbon and nitrogen
786 isotope heterogeneity in diamond: a new thermochronometer. Physics of the Earth and
787 Planetary Interiors 139, 35-43.
788 Komabayashi, T., Omori, S., 2006. Internally consistent thermodynamic data set for dense
789 hydrous magnesium silicates up to 35 GPa, 1600ºC: implications for water circulation in the
790 Earth's deep mantle. Physics of the Earth and Planetary Interiors 156, 89-107.
791 Lentz, D.R., 1999. Carbonatite genesis: A reexamination of the role of intrusion-related
792 pneumatolytic skarn processes in limestone melting. Geology 27, 335-338.
793 Li, X.-P., Rahn, M., Bucher, K., 2004. Serpentinites of the Zermatt-Saas ophiolite complex and
794 their texture evolution. Journal of Metamorphic Geology 22, 159-177.

795 Malavergne, V., Guyot, F., Wang, Y., Martinez, I., 1997. Partitioning of nickel, cobalt and
796 manganese between silicate perovskite and periclase: a test of crystal field theory at high
797 pressure. Earth and Planetary Science Letters 146, 499-509.
798 Masun, K.M., Scott Smith, B.H., 2008. The Pimenta Bueno kimberlite field, Rondônia, Brazil:
799 Tuffisitic kimberlite and transitional textures. Journal of Volcanology and Geothermal
800 Research 174, 81-89.
801 Mendelssohn, M.J., Milledge, H.J., 1995. Geologically significant information from routine
802 analysis of the mid-infrared spectra of diamonds. International Geology Reviews 37, 95-110.
803 Mibe, K., Kanzaki, M., Kawamoto, T., Matsukage, K.N., Fei, Y., Ono, S., 2007. Second critical
804 endpoint in the peridotite-H_2O system. Journal of Geophysical Research: Solid Earth 112,
805 B03201.
806 Moore, R.O., Gurney, J.J., Griffin, W.J., Shimizu, N., 1991. Ultra-high pressure garnet
807 inclusions in Monastery diamonds: trace element abundance patterns and conditions of origin.
808 European Journal of Mineralogy 3, 213-230.
809 Nestola, F., Burnham, A.D., Peruzzo, L., Tauro, L., Alvaro, M., Walter, M.J., Gunther, M.,
810 Kohn, S.C. (in press). Tetragonal Almandine-Pyrope Phase, TAPP: finally a name for it, the
811 new mineral jeffbenite. Mineralogical Magazine. doi: 10.1180/minmag.2016.080.059.Ohtani,
812 E., Litasov, K., Hosoya, T., Kubo, T., Kondo, T., 2004. Water transport into the deep mantle
813 and formation of a hydrous transition zone. Physics of the Earth and Planetary Interiors 143-
814 144, 255-269.
815 Peacock, S.M., 1990. Fluid processes in subduction zone. Science 248, 329-337.
816 Pearson, D.G., Brenker, F.E., Nestola, F., McNeill, J., Nasdala, L., Hutchison, M.T., Matveev,
817 S., Mather, K., Silversmit, G., Schmitz, S., Vekemans, B., Vincze, L., 2014. Hydrous mantle
818 transition zone indicated by ringwoodite included within diamond. Nature 507, 221-224.
819 Pietruszka, A.J., Norman, M.D., Garcia, M.O., Marske, J.P., Burns, D., 2013. Chemical
820 heterogeneity in the Hawaiian mantle plume from the alteration and dehydration of recycled
821 oceanic crust. Earth and Planetary Science Letters 361, 298-309.
822 Plá Cid, J., Nardi, L.V.S., Plá Cid, C., Enrique Gisbert, P., Balzaretti, N.M., 2014. Acid
823 compositions in a veined-lower mantle, as indicated by inclusions of (K,Na)-Hollandite + SiO_2
824 in diamonds. Lithos 196-197, 42-53.
825 Pokhilenko, N.P., Sobolev, N.V., Reutsky, V.N., Hall, A.E., Taylor, L.A., 2004. Crystalline
826 inclusions and C isotope ratios in diamonds from the Snap Lake/King Lake kimberlite dyke
827 system: evidence of ultradeep and enriched lithospheric mantle: Lithos 77, 57-67.
828 Robinson, D.N., 1979. Surface textures and other features of diamonds. Ph.D. Thesis, University
829 of Cape Town, 221 pp.
830 Sobolev N.V., Logvinova A.M., Zedgenizov D.A., Pokhilenko N.P., Kuzmin D.V., Sobolev
831 A.V., 2008. Olivine inclusions in Siberian diamonds: high precision approach to minor
832 elements. European Journal of Mineralogy 20, 305-315.
833 Sobolev, N.V., Logvinova, A.M., Zedgenizov, D.A., Pokhilenko, N.P., Malygina, E.V., Kuzmin,
834 D.V., Sobolev, A.V., 2009. Petrogenetic significance of minor elements in olivines from
835 diamonds and peridotite xenoliths from kimberlites of Yakutia. Lithos 112S, 701-713.
836 Stachel, T., 2001. Diamonds from the asthenosphere and the transition zone. European Journal
837 of Mineralogy 13, 883-892.
838 Stachel, T., Brey, G.P., Harris, J.W., 2000a. Kankan diamonds (Guinea) I: from the lithosphere
839 down to the transition zone. Contributions to Mineralogy and Petrology 140, 1-15.
840 Stachel, T., Harris, J.W., Brey, G.P., Joswig, W., 2000b. Kankan diamonds (Guinea) IIa: lower
841 mantle inclusion parageneses. Contributions to Mineralogy and Petrology 140: 16-27.
842 Stachel, T., Harris, J.W., Aulbach, S., Deines, P., 2002. Kankan diamonds (Guinea) IIaI: $\delta^{13}C$
843 and nitrogen characteristics of deep diamonds. Contributions to Mineralogy and Petrology 142,
844 465-475.

Stachel, T., Aulbach, S., Brey, G.P., Harris, J.W., Leost, I., Tappert, R., Viljoen, K.S., 2004. The trace element composition of silicate inclusions in diamonds: a review. Lithos 77, 1–19.

Stachel, T., Harris, J.W., 2008. The origin of cratonic diamonds – Constraints from mineral inclusions. Ore Geology Reviews 34, 5-32.

Stern, R.A, Palot, M. , Howell, D., Stachel, T. , Pearson, D.G. , Cartigny, P. , Oh, A., 2014. Methods and reference materials for SIMS diamond C- and N-isotope analysis. Canadian Centre for Isotopic Microanalysis, Research Report 14-01. University of Alberta, Education and Research Archive. http://hdl.handle.net/10402/era.38738

Sunagawa I., 1984. Morphology of natural and synthetic diamond crystals, in: Sunagawa, I. (Ed.), Materials science of the Earth's interior. Terra Scientific Publishing Company, Tokyo, Japan, pp. 303-330.

Tappert, R., Stachel, T., Harris, J.W., Muehlenbachs, K., Ludwig, T., Brey, G.P., 2005. Subducting oceanic crust: The source of deep diamonds. Geology 33, 565-568.

Taylor, W.R., Jaques, A.L., Ridd, M., 1990. Nitrogen-defect aggregation characteristics of some Australasian diamonds: Time-temperature constraints on the source regions of pipe and alluvial diamonds. American Mineralogist 75, 1290-1310.

Thomson, A.R., Kohn, S.C., Bulanova, G.P., Smith, C.B., Araujo, D., EIMF, Walter, M.J., 2014a. Origin of sub‐lithospheric diamonds from the Juina-5 kimberlite (Brazil): constraints from carbon isotopes and inclusion compositions. Contributions to Mineralogy and Petrology 168, 1081.

Thomson, A.R., Walter, M.J., Lord, O.T., Kohn, S.C., 2014b. Experimental determination of melting in the systems enstatite-magnesite and magnesite-calcite from 15 to 80 GPa. American Mineralogist 99, 1544-1554.

Thomson, A.R., Walter, M.J., Kohn, S.C., Brooker, R.A., 2016. Slab melting as a barrier to deep carbon subduction. Nature 529, 76-79.

Thomson et al. (*this issue*). Trace element composition of silicate inclusions in Juina-5 diamonds: evidence for diamond growth from slab melts. [Details to be added post-review]

Tompkins, L.A., Gonzaga, G.M., 1989. Diamonds in Brazil and a proposed model for the origin and distribution of diamonds in the Coromandel Region, Minas Gerais, Brazil. Economic Geology 84, 591-602.

Turekian, K.K., Wedepohl, K.H., 1961. Distribution of elements in some major units of the Earth's crust. Geological Society of America Bulletin 72, 175-192.

Vance, E.R., Milledge, H.J., 1972. Natural and laboratory α-particle irradiation of diamond. Mineralogical Magazine 38, 878-881.

Walter, M.J., Bulanova, G.P., Armstrong, L.A., Keshav, S., Blundy, J.D., Gudfinnsson, G., Lord, O.T., Lennie, A.R., Clark, S.M., Smith, C.B., Gobbo, L., 2008. Primary carbonatite melt from deeply subducted oceanic crust. Science454, 622–625.

Walter, M.J., Kohn, S.C., Araujo, D., Bulanova, G.P., Smith, C.B., Gaillou, E., Wang, J., Steele, A., Shirey, S.B., 2011. Deep mantle cycling of oceanic crust: evidence from diamonds and their mineral inclusions. Science 334, 54-57.

Wang, W.Y., Sueno, S., Takahashi, E., Yurimoto, H., Gasparik, T., 2000. Enrichment processes at the base of the Archean lithospheric mantle: observations from trace element characteristics of pyropic garnet inclusions in diamonds. Contributions to Mineralogy and Petrology 139, 720-733.

Wiser, N.M., Wood, B.J., 1991. Experimental determination of activities in Fe-Mg olivine at 1400 K. Contributions to Mineralogy and Petrology 108, 146-153.

Wood, B.J., 2000. Phase transformations and partitioning relations in peridotite under lower mantle conditions. Earth and Planetary Science Letters 174, 341-354.

Woods, G.S., 1986. Platelets and the infrared absorption of type Ia diamonds. Proceedings of the Royal Society of London 407, 219-238.

Zedgenizov, D.A., Kagi, H., Shatsky, V.S., Ragozin, A.L., 2014a. Local variations of carbon isotope composition in diamonds from São-Luis (Brazil): Evidence for heterogenous carbon reservoir in sublithospheric mantle. Chemical Geology 363, 114-124.
Zedgenizov, D.A., Shatskiy, A., Ragozin, A.L., Kagi, H., Shatsky, V.S., 2014b. Merwinite in diamond from São Luiz, Brazil: A new mineral of the Ca-rich mantle environment. American Mineralogist 99, 547-550.
Zedgenizov, D.A., Shatsky, V.S., Panin, A.V., Evtushenko, O.V., Ragozin, A.L., Kagi, H., 2015. Evidence for phase transitions in mineral inclusions in superdeep diamonds of the São Luiz deposit (Brazil). Russian Geology and Geophysics 56, 296-305.
Zhang, Y., 2010. Diffusion in minerals and melts: theoretical background, in: Zhang, Y. and Cherniak, D.J. (Eds.), Reviews in Mineralogy and Geochemistry Volume 72: Diffusion in Minerals and Melts. Mineralogical Society of America, pp. 5-59.

Figure captions

Fig. 1 a) Map of Brazil showing cratonic (Transamazonian , i.e. >2 Ga) areas (wavy lines) and selected kimberlite and diamond occurrences (B – Batovi, C – Coromandel, J – Juina-5, MR – Machado River), b) simplified geological map of the source region for the samples, and c) schematic cross section.

Fig. 2. Morphology of Machado River diamonds: a) high quality, mostly white, good shapes (70% dodecahedra, 30% octahedra); b) rhombic cleavage cracks and percussion marks indicating a strong alluvial abrasion history; c) diamond with notable percussion marks; d) green and brown radiation spots implying a history of burial at enhanced temperature (colour in online version). (These samples were not studied further.) Scale bars are 1 mm.

Fig. 3. Cathodoluminescence images of diamonds. a) P7 (peridotitic diamond containing an olivine inclusion) has predominantly sharp octahedrally-faceted oscillatory and sector zoning, and a bright sector of cuboid growth in the bottom right. b) P28 (superdeep suite containing a composite Ca-walstromite + diopside inclusion) has weak diffuse zoning running left to right overprinted by a mesh- or web-like texture of uncertain origin. The near-vertical linear features perpendicular to the diffuse zoning are polishing scratches. c) P30 (superdeep diamond containing a ferropericlase inclusion) has a complex core and diffuse oscillatory zoning overprinted by occasional wrinkle-like textures. d) P43 (inclusion-free) has complex irregular core textures overgrown by sharp octahedrally-faceted oscillatory zoning. Scale bars are 1 mm; brightness and contrast settings vary between images. The overlain rectangle in (c) indicates the area shown in detail in Fig. 10a.

Fig. 4. Backscattered electron images of composite inclusions in situ within the diamonds: a) olivine (light grey) + orthopyroxene (medium grey) inclusion in P20; b) Ca-walstromite (light grey) + diopside (dark grey) inclusion in P28. (The powder-like material in very dark grey at the top and bottom of the inclusion is polishing debris.) Scale bars are 30 μm.

Fig. 5. Representative FTIR spectra from discrete growth zones in a) diamond P16, showing a Type IaB core with an intense absorption band at 3107 cm^{-1}, Type IIa intermediate zone and Type IaA rim, and b) diamond P43, showing a low-N and irregular (platelet-degraded) Type IaB core and a medium-N and regular rim. Spectra are offset for clarity; abbreviations as in Table 5.

Fig. 6. Olivine inclusion compositions at Machado River compared to the worldwide distribution of harzburgitic and lherzolitic olivine inclusions (data from Stachel and Harris,

2008) and the narrow distributions for two Siberian kimberlite fields (data from Sobolev et al., 2009).

Fig. 7. Comparison of Machado River mineral inclusions to other superdeep diamond occurrences. a) Major element compositions of ferropericlase at Machado River (black circles) and other localities (data from the compilation in Thomson et al., 2016). b) Major element compositions of majorite garnet at Machado River (black circles) and other localities (data from the compilation in Kiseeva et al., 2013). c) Primitive mantle-normalised REE concentrations in majorite at Machado River (solid line) and other localities (sources: Jagersfontein – Tappert et al., 2005; Monastery – Moore et al., 1991; Collier-4 – Bulanova et al., 2010, lower boundary estimated). d) Primitive mantle-normalised REE concentrations in former $CaSiO_3$ perovskite in diamonds from Machado River (solid lines), and other localities (Collier-4 – Bulanova et al., 2010; São Luiz – Harte et al., 1999; Kankan – Stachel et al., 2000b).

Fig. 8 Nitrogen concentration as a function of aggregation state for Machado River diamonds. Dotted lines are calculated isotherms for a model 1.5 Ga mantle residence using the rate equation of Taylor et al. (1990). Dashed lines show core-rim relationships on strongly zoned samples (labelled; in all cases the rim is less aggregated than the core).

Fig. 9. Distribution of carbon isotopic compositions of diamonds from Machado River (superdeep and unknown parageneses), Juina-5 (Thomson et al., 2014), Collier-4 (Bulanova et al., 2010), Juina-region alluvials (Hutchison et al., 1999; Kaminsky et al., 2001; Zedgenizov et al., 2014a), Jagersfontein (Deines et al.,1991; Tappert et al., 2005) and Kankan (Stachel et al., 2002). The average mantle range is shown in grey.

Fig. 10. a) Detailed cathodoluminescence image of part of diamond P30 (see Fig. 3c for location) showing width and orientation of lines used to extract intensity profiles, and b) CL intensity profiles (arbitrary greyscale values) and fits to the diffusion equation.

Fig. 11. Summary of classification of diamonds (details provided in Table 5). SD – considered superdeep on the basis of their inclusions (n = 10); SD? – inferred superdeep on the basis of N aggregation and CL textures (n = 3); * – core assigned to class SD? and rim assigned to class L(P) (n = 1); LP – considered peridotitic (lithospheric) on the basis of their inclusions (n = 7); LE – considered eclogitic (lithospheric) on the basis of their inclusions (n = 5); L? – inferred lithospheric on the basis of N aggregation and CL textures (n = 10); ? – of unknown paragenesis because of insufficient data (n = 9).

Table 1. Electron probe microanalysis (EPMA) data for silicate and oxide diamond inclusions and estimated bulk compositions of polyphase inclusions. SiO_2 inclusions P23-1 and P34-1 were not analysed. Abbreviations: bulk – estimated bulk composition (normalised); Ca-wa – Ca-walstromite; di – diopside; dol – dolomite; fper – ferropericlase; gt – garnet; jbt – jeffbenite; ksp – K-feldspar; mer – merwinite; ol – olivine; omph – omphacite; opx – orthpyroxene.

	P2-1 ksp	P2-2[1] ksp	P3 omph	P4-1a Ca-wa	P4-1b di	P4-1 bulk	P4-2a mer	P4-2b di	P4-2 bulk	P7 ol	P9 ol	P11-1 fper
SiO_2	65.72	69.41	55.60	49.60	51.16	51.25	34.85	52.79	38.29	39.81	40.88	0.06
TiO_2	0.25	0.22	0.06	0.04	0.13	0.06	0.03	0.19	0.05	<0.02	0.02	<0.02
Al_2O_3	15.17	10.36	6.90	0.03	2.48	0.53	0.07	0.33	0.11	0.03	0.03	0.06

Cr_2O_3	0.01	0.01	0.14	0.03	0.33	0.09	0.10	0.16	0.11	0.03	n.a.	0.19
FeO	1.3	1.04	2.61	0.16	2.15	0.57	2.28	1.97	2.29	7.81	5.62	19.90
MnO	0.03	0.04	0.01	0.04	0.08	0.05	0.04	0.04	0.04	0.09	0.08	0.18
MgO	0.25	0.16	12.61	0.36	15.87	3.55	11.83	17.86	12.99	52.11	52.43	76.57
CaO	0.63	1.92	18.58	46.86	26.21	43.88	47.97	24.95	45.86	0.04	0.02	<0.02
Na_2O	0.21	0.22	2.52	<0.02	0.13	0.03	0.14	0.04	0.13	<0.02	<0.02	<0.02
K_2O	12.49	8.81	0.27	<0.02	<0.02	<0.02	0.01	0.00	<0.02	<0.02	n.a.	<0.02
NiO	0.03	n.a.	0.05	<0.02	<0.02	<0.02	0.11	0.14	0.12	0.40	0.34	1.25
Total	96.09	94.47	99.34	97.11	98.54	100	97.42	98.47	100	100.32	99.42	98.22

990

	P11-6 di	P11-7 opx	P11-8 di	P11-9 fper	P12-1 fper	P12-2 fper	P14-1 opx	P14-2 ol	P15-1 fper	P15-2 ?dol	P15-3 fper	P15-4 opx
SiO_2	54.33	60.72	55.59	0.03	0.06	0.03	55.57	40.51	0.07	1.51	n.a.	58.19
TiO_2	0.07	<0.02	0.07	<0.02	<0.02	<0.02	0.02	<0.02	<0.02	<0.02	n.a.	<0.02
Al_2O_3	0.12	0.19	0.12	<0.01	0.07	0.02	0.52	<0.02	0.06	0.04	n.a.	1.02
Cr_2O_3	0.13	0.23	0.14	0.11	0.25	0.25	0.25	0.02	0.69	0.05	0.36	0.44
FeO	1.38	2.31	1.48	13.22	20.74	20.61	8.13	9.67	19.44	5.91	19.02	3.18
MnO	0.05	0.11	0.05	0.14	0.09	0.09	0.18	0.09	0.16	0.16	0.12	0.11
MgO	17.62	37.17	18.13	56.50	76.78	76.84	30.35	48.37	79.07	33.38	78.51	37.41
CaO	25.58	0.04	25.61	0.02	<0.02	<0.02	0.84	0.01	0.01	17.82	n.a.	0.15
Na_2O	<0.01	<0.02	<0.02	0.02	0.13	0.13	<0.02	0.05	0.03	0.31	0.13	0.05
K_2O	<0.03	<0.02	0.02	<0.02	<0.02	<0.02	0.02	<0.02	<0.02	0.05	n.a.	n.a.
NiO	<0.04	<0.02	0.04	0.88	1.35	1.27	0.05	0.37	1.11	0.16	1.43	0.00
Total	99.28	100.78	101.25	70.93	99.47	99.24	95.93	99.09	100.62	59.39	99.57	100.5

991

	P21-1 ?dol	P21-2a gt	P21-2b di	P21-2 bulk	P23 gt	P24-1 gt	P24-2 omph	P27 omph	P28-1a di	P28-1b Ca-wa	P28-1 bulk	P29-1 omph
SiO_2	0.05	41.48	52.99	46.05	49.13	40.11	55.86	55.86	53.35	49.98	51.41	55.
TiO_2	0.00	0.87	0.25	0.62	0.42	0.38	0.57	0.57	0.04	0.03	0.03	0.
Al_2O_3	0.05	22.25	3.79	14.86	12.41	21.34	9.17	9.17	1.12	0.04	0.20	10.
Cr_2O_3	<0.02	0.05	0.01	0.03	0.21	<0.02	0.09	0.09	0.14	<0.04	0.03	0.
FeO	0.27	5.02	2.17	3.88	5.14	11.13	6.29	6.29	1.22	0.16	0.32	4.
MnO	0.08	0.11	0.04	0.08	0.31	0.16	0.08	0.08	0.07	0.02	0.03	0.
MgO	18.72	13.07	16.50	14.43	24.62	9.25	9.59	9.59	16.24	0.49	2.83	9.
CaO	25.21	17.64	23.57	20.00	8.14	14.57	11.80	11.80	26.51	47.22	45.05	13.
Na_2O	<0.02	<0.02	0.04	0.02	0.30	0.13	4.90	4.90	0.06	0.04	0.04	5.
K_2O	0.11	<0.02	0.05	0.02	<0.04	0.09	0.19	0.19	0.04	0.08	0.08	0.
NiO	n.a.	0.01	0.03	0.02	<0.07	<0.04	<0.02	<0.02	<0.04	<0.04	<0.04	<0.04
Total	44.49	100.50	99.44	100	100.68	97.17	98.55	98.55	98.78	98.06	98.16	100.

992

	P33-2 ol	P34-2 fper	P37-1 opx	P40-1 ol	P41-1 ol
SiO_2	40.48	8.97	57.56	42.79	42.03
TiO_2	0.05	<0.02	<0.02	<0.02	<0.02
Al_2O_3	0.77	8.38	0.66	0.03	0.04
Cr_2O_3	0.01	0.76	0.47	0.17	0.09
FeO	8.66	18.57	3.67	5.14	6.00
MnO	0.09	0.23	0.09	0.07	0.07
MgO	41.52	61.45	35.66	52.15	50.01
CaO	0.22	0.03	0.17	0.02	0.01
Na_2O	0.07	0.64	0.09	0.06	<0.02
K_2O	0.24	0.35	0.10	<0.02	<0.02
NiO	<0.02	1.20	0.13	0.29	0.39
Total	92.12	100.59	98.59	100.73	98.63

1 - contains 2.28 % P_2O_5.

Table 2. Electron probe microanalysis (EPMA) data for sulphide inclusions (those in diamonds P6, P8 and P10 were analysed by EDS only because of their small size). '-' – not analysed.

	P5	P17	P27
Fe	39.28	54.49	52.83
Ni	20.37	1.22	2.71
Co	0.36	0.07	0.28
Cu	1.19	1.13	3.27
Zn	<0.01	0.01	-
Cr	-	-	<0.01
S	36.66	38.33	37.87
Total	97.87	95.24	96.96

Table 3. Trace element concentrations in inclusions, as determined by SIMS. Abbreviations: omph – omphacite; opx – orthopyroxene; fper – ferropericlase; b.d.l. – below the detection limit; '-' – not analysed.

	P3 omph	P4-1 composite	P4-2 composite	P7 olivine	P9 olivine	P12[2] fper	P14 olivine
Li	9.62	-	-	0.98	3.43	25.5	1.63
Na	20200	-	-	131	260	8578	111
P	36.5	-	-	28.1	44.7	2.0	51.7
K	2078	-	-	72	358	1	106
Ca	126000	252000	172000	312	319	-	627
Sc	12	18	17	3.6	2.8	4.6	4.3
Ti	371	-	-	56	19	12	28
V	241	-	-	5.8	9.7	36.5	7.4
Cr	0.16	-	-	247	593	-	280
Mn	344	-	-	667	556	1011	917
Co	44	-	-	107	87	440	133
Co[1]	33	-	-	106	87	376	134
Ni[1]	178	-	-	2800	2250	5000	2880
Cu[1]	79	-	-	3	158	35	0.7
Zn[1]	13	-	-	44	25	b.d.l.	65
Ga[1]	7.4	-	-	0.12	0.16	0.9	0.08
Rb	3.0	-	-	-	-	1.7	-
Sr	316	52.4	14.6	0.52	1.20	0.57	0.79
Y	0.31	8.53	1.16	0.08	0.41	0.02	0.10
Zr	1.38	17.4	11.8	0.38	0.94	0.06	0.48
Nb	0.84	0.08	0.35	0.05	0.24	0.02	407
Mo	0.05	-	-	-	-	0.12	-
Sn	20.1	-	-	57	341	7.8	419
Cs	0.11	-	-	-	-	b.d.l.	-
Ba	26.4	7.53	18.4	1.17	10.13	0.09	191
La	6.06	1.03	0.65	0.11	0.25	0.20	0.39
Ce	15.5	1.53	0.68	0.12	0.20	0.05	0.48
Pr	1.62	0.23	0.09	-	-	0.02	-
Nd	4.67	2.96	0.88	-	-	b.d.l.	-
Sm	0.59	0.87	0.40	-	-	b.d.l.	-
Eu	0.10	0.59	0.05	-	-	b.d.l.	-
Gd	0.45	1.84	0.32	-	-	b.d.l.	-
Tb	0.04	0.41	0.08	-	-	b.d.l.	-
Dy	0.20	2.65	0.28	-	-	b.d.l.	-

Ho	b.d.l.	0.43	0.07	-	-	b.d.l.	-
Er	0.14	1.22	0.20	-	-	b.d.l.	-
Tm	0.02	0.18	0.05	-	-	b.d.l.	-
Yb	b.d.l.	2.08	0.32	-	-	0.13	-
Lu	b.d.l.	0.22	0.04	-	-	b.d.l.	-
Hf	b.d.l.	0.60	0.59	-	-	b.d.l.	-
Ta	0.04	-	-	-	-	b.d.l.	-
Th	0.11	0.03	0.09	-	-	0.01	-
U	0.02	0.02	0.30	-	-	b.d.l.	-

Table 3 (cont.)

	P14 opx	P15 opx[3]	P20 opx[3]	P21 majorite
Li	0.30	-	0.92	0.60
Na	527	-	459	26.2
P	6.1	-	43.9	83.7
K	627	-	6	9
Ca	5040	5640	977	108000
Sc	5.70	12	22	22
Ti	132	-	464	4132
V	41.3	-	279	121
Cr	0.28	-	0.45	0.07
Mn	1643	-	4587	994
Co	101	-	17	19
Co[1]	75	-	15	15
Ni[1]	301	-	39	24
Cu[1]	4	-	5	0.8
Zn[1]	30	-	126	24
Ga[1]	2.2	-	1.9	17
Rb	37.5	-	0.1	0.01
Sr	3.88	0.20	0.02	1.11
Y	0.03	0.01	0.03	41.4
Zr	0.34	1.92	1.87	363
Nb	78.8	0.04	0.05	5.24
Mo	0.03	-	0.01	0.08
Sn	3.4	-	8.99	22.6
Cs	2.18	-	0.04	0.09
Ba	1217	0.07	0.50	0.58
La	2.42	0.03	0.10	1.51
Ce	2.59	b.d.l.	0.08	12.7
Pr	0.34	0.02	0.01	3.19
Nd	0.67	0.05	0.09	25.1
Sm	2.35	0.03	0.02	8.06
Eu	b.d.l.	0.02	b.d.l.	1.88
Gd	b.d.l.	0.03	0.02	6.17
Tb	0.03	0.01	b.d.l.	1.17
Dy	0.64	0.04	b.d.l.	7.78
Ho	b.d.l.	0.01	b.d.l.	1.31
Er	b.d.l.	0.04	b.d.l.	3.59
Tm	0.05	b.d.l.	b.d.l.	0.67
Yb	1.31	0.16	b.d.l.	4.67
Lu	0.82	0.01	b.d.l.	0.55
Hf	0.64	0.14	0.05	8.87
Ta	2.00	-	b.d.l.	0.70
Th	0.23	0.02	b.d.l.	1.48
U	b.d.l.	0.07	b.d.l.	1.33

1 – data acquired at high mass resolution. 2 – trace Si present at ~ 2 ppm. 3 – retrogressed bridgmanite.

1012 Table 4. Trace element concentrations in Ca-walstromite of diamond P28, as determined by
1013 LA-ICP-MS. All values in ppm except CaO (wt%); b.d.l. = below the detection limit.
1014

	Concentration	Det. Lim.
Li	b.d.l.	1.73
Na	24	5
Mg	6283	0.3
Al	400	0.2
P	30	2
K	496	2
CaO	48.3	0.0022
Sc	14.9	0.01
Ti	158	0.1
As	b.d.l.	0.29
Rb	b.d.l.	0.02
Sr	573	0.001
Y	9.56	0.003
Zr	64.0	0.002
Nb	0.017	0.002
Cs	0.130	0.010
Ba	0.418	0.016
La	38.0	0.001
Ce	77.4	0.001
Pr	9.28	0.001
Nd	39.1	0.005
Sm	6.95	0.005
Eu	1.88	0.001
Gd	5.32	0.005
Tb	0.564	0.001
Dy	2.76	0.003
Ho	0.386	0.001
Er	0.857	0.002
Tm	0.100	0.001
Yb	0.561	0.008
Lu	0.089	0.001
Hf	1.601	0.010
Ta	0.002	0.001
Th	2.75	0.001
U	0.27	0.001

1015
1016

Table 5. Nitrogen concentrations, aggregation states and platelet characteristics (D = platelet degradation observed) as determined by FTIR. Abbreviations: c – core, i – intermediate, r – rim; b.d.l. – below the detection limit (1 – 5 ppm depending on the quality of the spectrum), n.a. – not analysed. Classes: SD – considered superdeep on the basis of their inclusions, SD? – inferred superdeep on the basis of N aggregation and CL textures, LP – considered lithospheric (peridotitic) on the basis of their inclusions, LE – considered lithospheric (eclogitic) on the basis of their inclusions, L? – inferred lithospheric on the basis of N aggregation and CL textures, ? – of unknown paragenesis because N < 4 ppm (or not measured) and inclusions not observed.

Sample	Class	Platelet	$[N_{total}]$	%IaB	Sample	Class	Platelet	$[N_{total}]$	%IaB
P1	?		b.d.l.		P24	L(E)		384	5
P2	L?		867	3	P25	L?		514	46
P3	L(E)		193	67	P26	L?		908	40
P4	SD		b.d.l.		P27	L(E)		733	30
P5	L(P)		437	16	P28	SD	D	25	100
P6	SD?	D	54	95	P29	L(E)		564	11
P7	L(P)		1650	14	P30	SD		b.d.l.	
P8	?		b.d.l.		P31	L?		1136	1
P9	L(P)		237	70	P32	?		b.d.l.	
P10	SD?	D	80	100	P33	SD	D	b.d.l.	
P11	SD		b.d.l.		P34	SD		b.d.l.	
P12	SD	D	41	100	P35	?		n.a.	
P13	?		b.d.l.		P36	?		b.d.l.	
P14	L(P)		457	48	P37	L(P)		592	33
P15	SD		b.d.l.		P38	L?		941	51
P16-c	L(P)		493	97	P39	?		b.d.l.	
P16-i	"		18	72	P40-c	SD?	D	230	100
P16-r	"		246	16	P40-r	L(P)		b.d.l.	
P17	L(E)		733	93	P41	L(P)		984	90
P18	L?		1020	2	P42-c	L?		421	74
P19	L?		841	2	P42-r	L?		356	24
P20	SD		b.d.l.		P43-c	SD?	D	34	100
P21	SD		b.d.l.		P43-r	"	D	310	97
P22	?		b.d.l.		P44	L?		1369	9
P23	SD		b.d.l.		P45	L?		200	61

Table 6. Carbon isotopic compositions ($\delta^{13}C$) of the diamonds. Values in parentheses are 1σ of multiple analyses in terms of the last significant figure; for single analyses the uncertainty is assumed to be 0.1‰ except where the standard error of the counting statistics is greater (indicated in square brackets). For some samples zoning is absent or complex and the terms "core", "int." (intermediate) and "rim" may not coincide with the growth geometry.

Sample	$\delta^{13}C$	Comment	Sample	$\delta^{13}C$	Comment
P03	-18.5(2)	core (average of 3 analyses)	P17 (cont'd)	-9.1(3)	rim (average of 4 analyses); 3 int. points with int. values
"	-16.3	intermediate	P19	-4.0(1)	3 analyses, "core" to "rim"
"	-18.2	intermediate	P20	-15.2	core
"	-13.7	rim	"	-18.3(1)	4 analyses, int. to rim
P04	-2.4(1)	6 analyses, core to rim	P21	-1.4(3)	13 analyses (range = -1.8 to -0.9); no obvious trend
P07	-5.16(1)	3 analyses, core to rim	P23	-7.8(1.6)	3 analyses (range = -5.9 to -8.9); no obvious trend
P08	-10.8	core	P28	-2.9(1)	8 analyses in all zones
"	-11.0	intermediate	P30	-5.3(2)	10 analyses from core to rim
"	-11.1	rim	P31	-2.8(2)	3 analyses core to rim
P09	-4.6(7)	5 analyses (range = -3.6 to -5.3) with no obvious trend	P32	-2.3(1)	2 analyses, core and rim
P10	-4.86(5)	3 analyses, core to rim	P33	-3.9(2)	three analyses core to rim
P11	-0.5	core	P34	-5.5(1)	2 analyses, core and rim
"	-1.5	intermediate	P36	-4.8	core; 2 int. points with int. values
"	-0.8	rim	"	-3.9[2]	rim
"	-0.3	rim	P39	-4.3(1)	average of 3 analyses core to rim; one int. point of -5.1
P12	-1.8(1)	6 analyses, intermediate to rim	P40	-4.6(2)	three analyses core to rim
P14	-4.8	core	P41	-4.5	single measurement at rim
"	-3.5	rim; 3 int. points with int. values	P42	-6.1	core; 1 int. point with int. value
P15	-2.0(1)	5 analyses; rim slightly (~0.25 ‰) heavier than core	"	-4.8[2]	rim
P16	-6.2	core	P43	-5.6[2]	core; 5 int. points with int. values
"	-4.7	rim; 1 int. point with int. value	"	-7.1	rim
P17	-11.8(1.0)	core (average of 3 analyses)	P44	-7.6(2)	three analyses core to rim

Figure 1

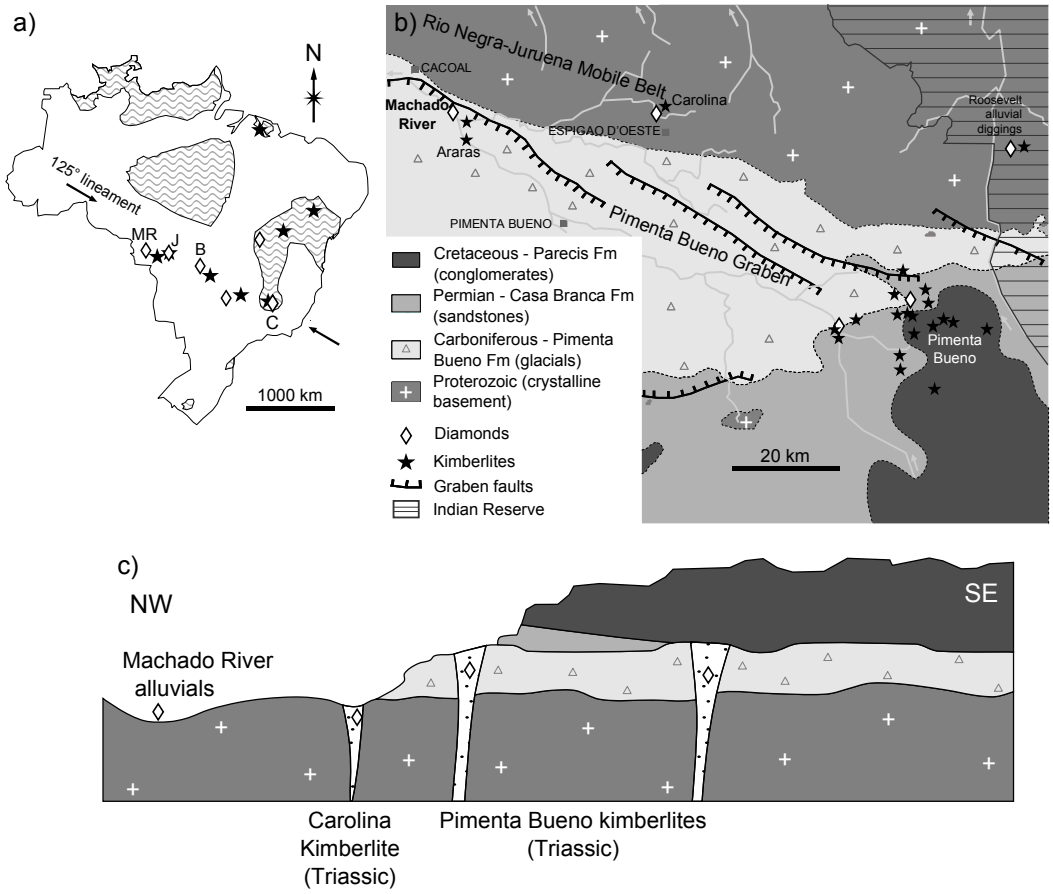

Figure 2

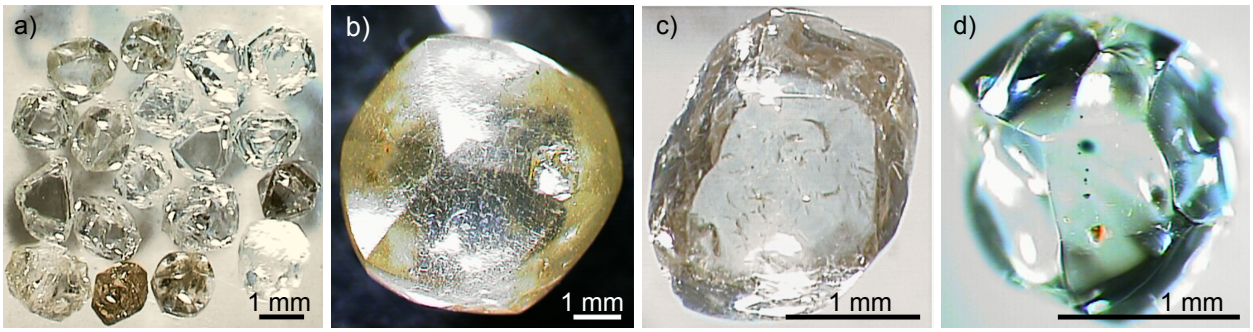

Figure 3

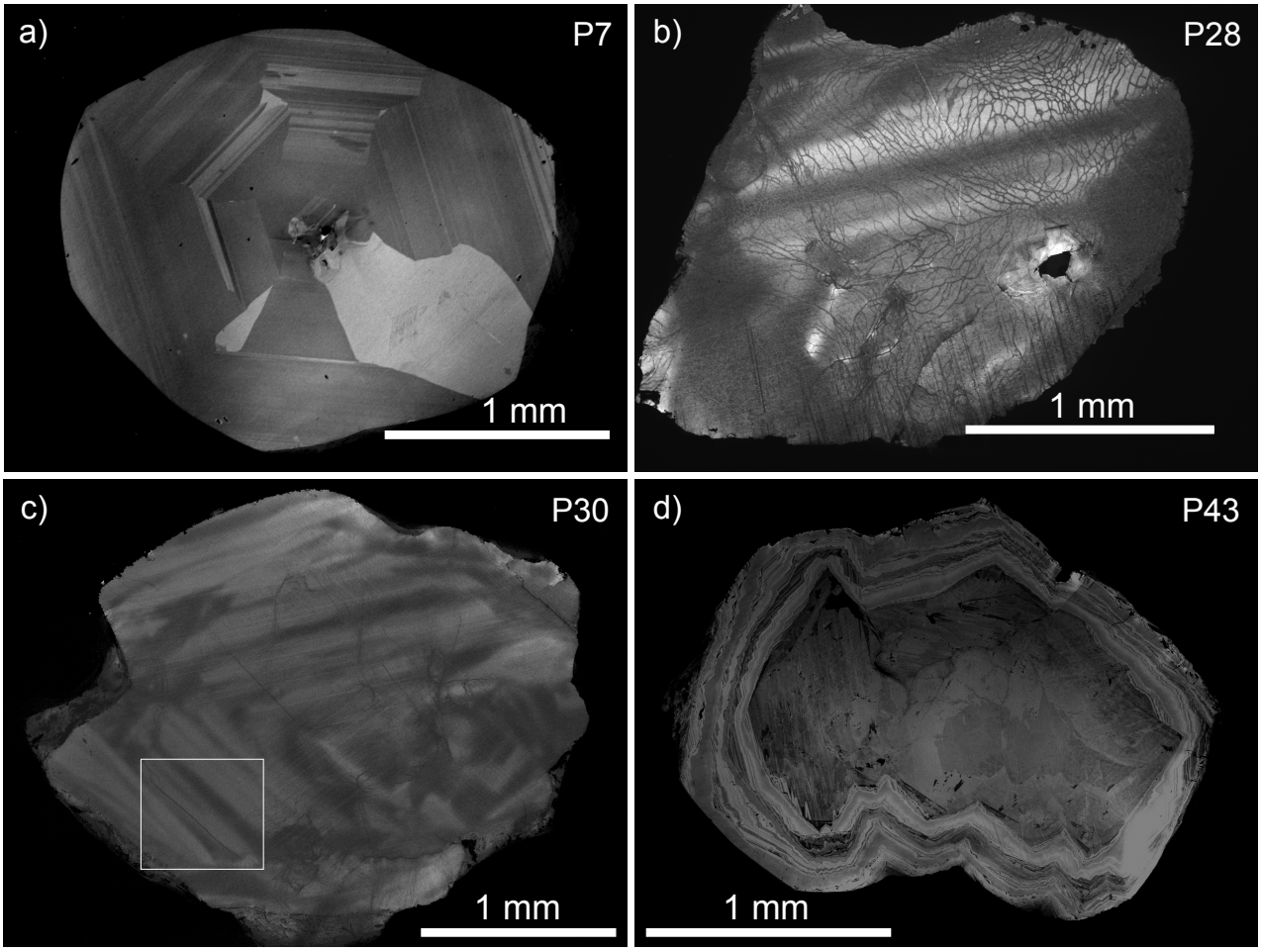

Figure 4

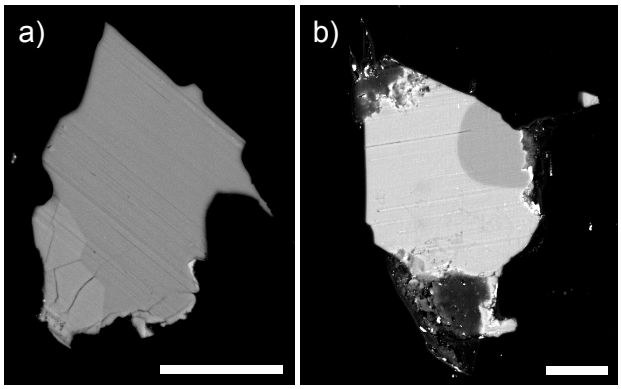

Figure 5

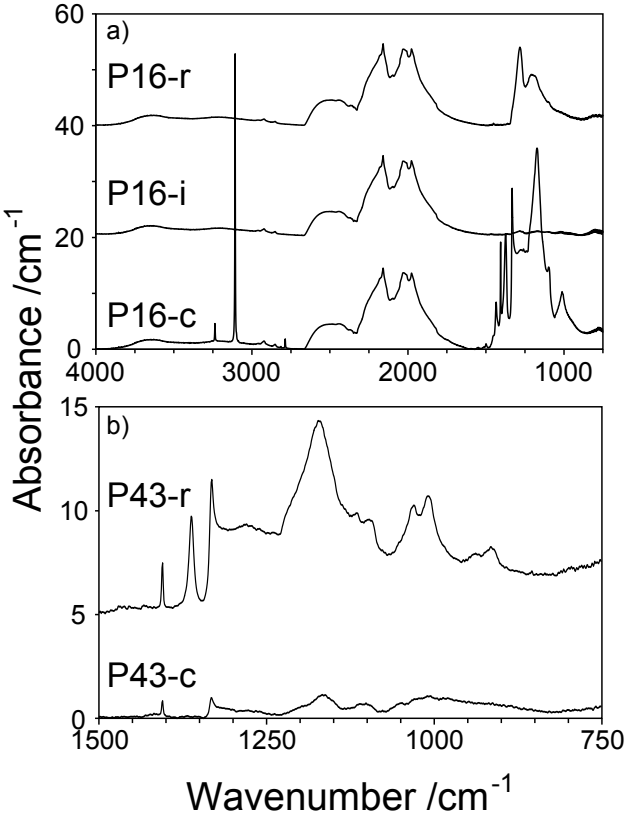

Figure 6

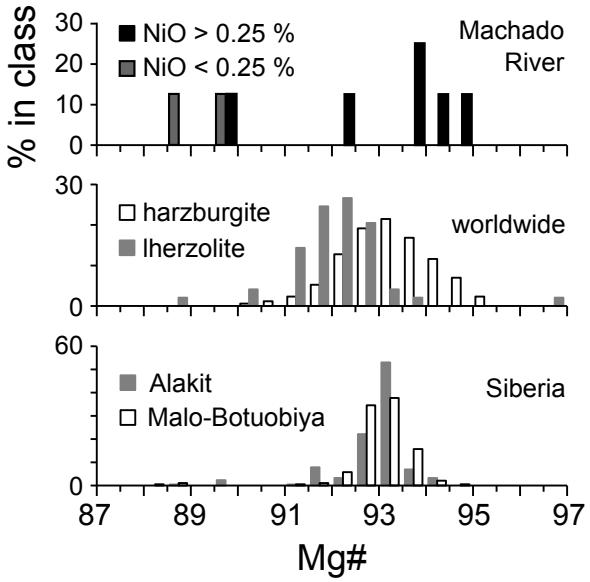

Figure 7

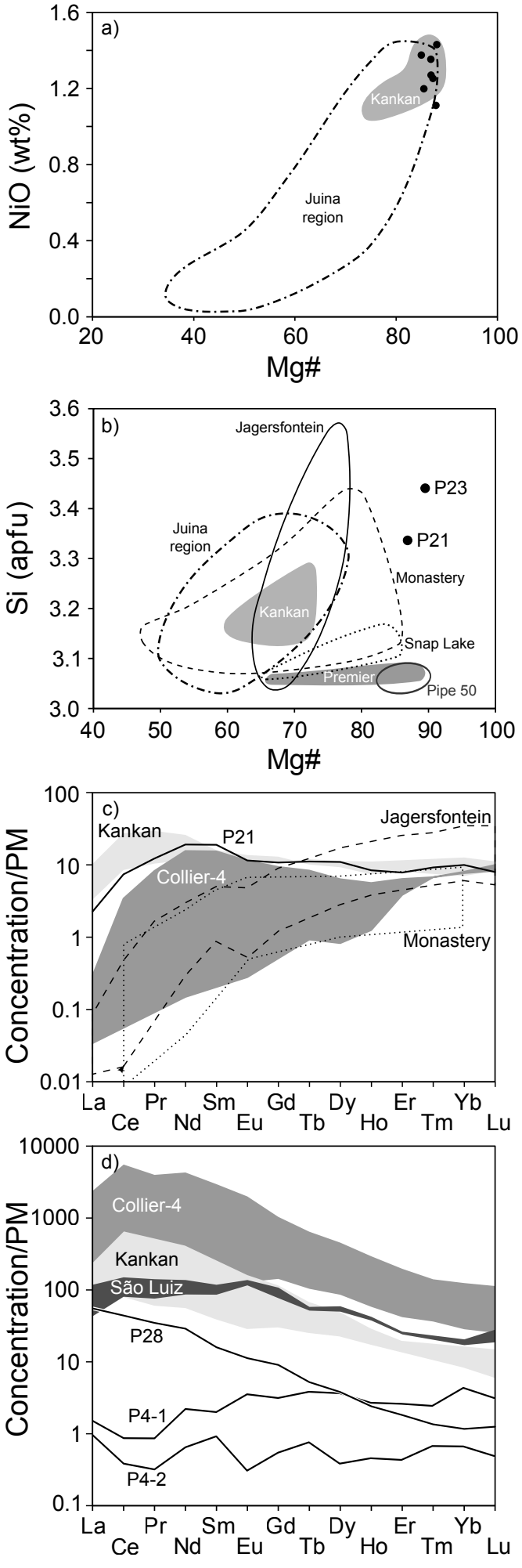

Figure 8

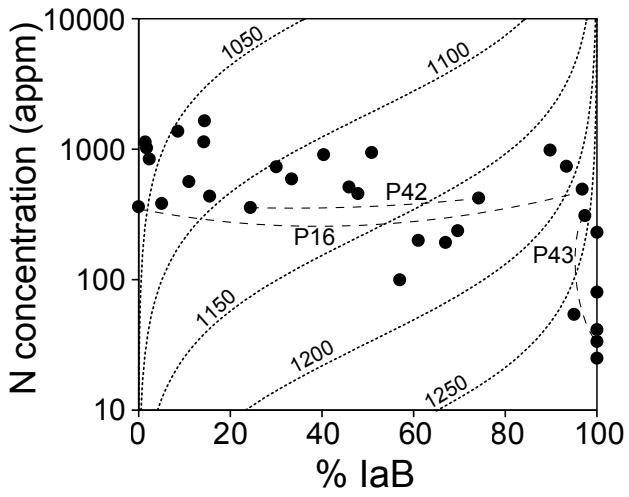

Figure 9

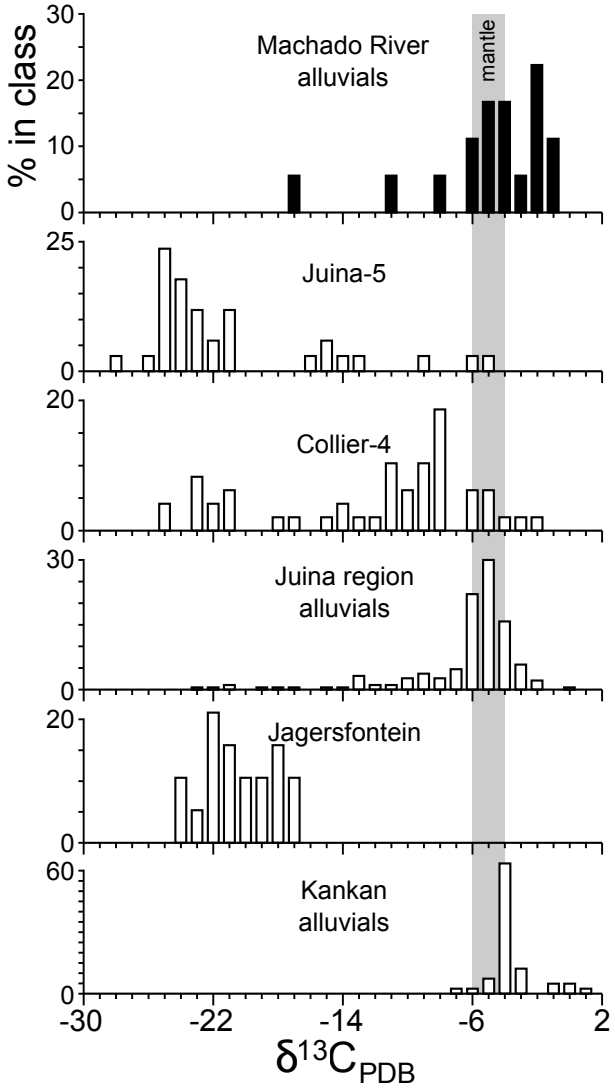

Figure 10

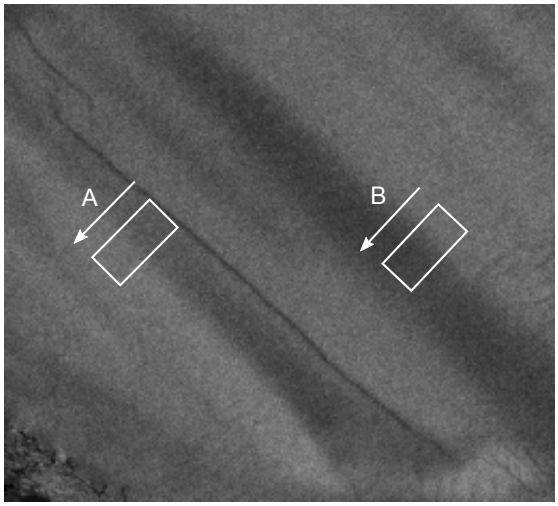

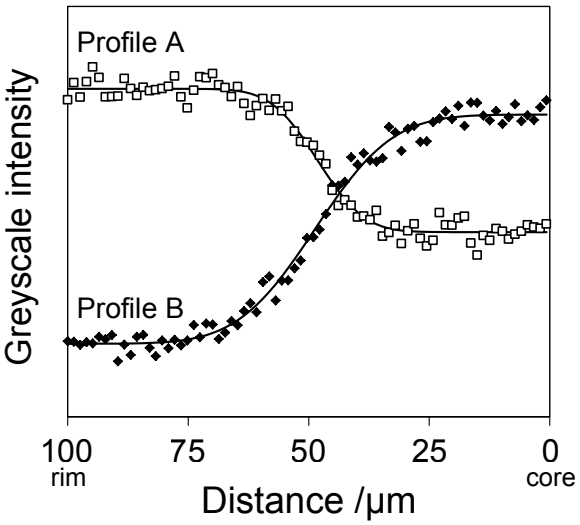

Figure 11